On-axis afocal telescopes as framework for CubeSat based astronomical imagers and slit-less spectrographs

ANWESH KUMAR MISHRA[1,*] , GOURAV BANERJEE[1,2], REKHESH MOHAN[1] and MAHESWAR GOPINATHAN[1]

[1]Indian Institute of Astrophysics, Koramangala, Bangalore 560034, India.
[2]Vainu Bappu Observatory, Kavalur 635701, India.
*Corresponding author. E-mail: mishraanwesh@gmail.com

Abstract. CubeSats present unique opportunities for observational astronomy in the modern era. They are useful in observing difficult-to-access wavelength regions and long-term monitoring of interesting astronomical sources. However, conventional telescope designs are not necessarily the best fit for the restricted envelope of a CubeSat. Additionally, fine-pointing stability on these platforms is difficult due to the low mass of the spacecraft, and special allocations within the optical design are needed to achieve stable pointing. We propose afocal telescope designs as the framework to realise imagers and low-resolution spectrographs on CubeSat platforms. These designs help reduce the number of components in the optical chain and aim to improve throughput and sensitivity compared to conventional designs. Additionally, they also provide a fine steering mechanism within a collimated beam section. Fine beam steering within the collimated beam section avoids issues of image degradation due to out-of-plane rotation of the image plane or offset in the rotation axis of the mirror. This permits using simple and mostly off-the-shelf tip-tilt mirrors for beam steering. The designs discussed here also allow for a standard telescope design to be used in many instrument types; thus reducing the complexity as well as the development time and cost. The optical design, performance, and SNR estimations of these designs, along with some interesting science cases, are discussed. Several practical aspects in implementation, such as guiding, tolerancing, choice of detectors, vibration analysis, and laboratory test setups, are also presented.

Keywords. Optical design—CubeSat—fine steering mirror—astronomical instrumentation.

1. Introduction: Astronomy with CubeSats

In recent years, there has been remarkable progress in the technology and application of small satellites for both commercial and scientific use (Poghosyan & Golkar 2017). Particularly, the CubeSat format and standardisation have been quite popular in terms of the number of satellites launched and planned (Liddle *et al.* 2020). CubeSat-based observations from a Low Earth Orbit can complement ground-based observations (Shkolnik 2018) in terms of uninterrupted wavelength coverage (e.g., 150–2500 nm) and good temporal coverage. This would be particularly interesting for monitoring of variable stars, such as pulsating or flaring types. Similarly, science cases, such as asteroseismology (Nowak *et al.* 2016) and exoplanet studies (Pong 2018), which require very long and uninterrupted

observing runs, can greatly benefit from CubeSat missions operating in sun-synchronous orbits.

At the same time, CubeSats can achieve these goals with significantly smaller mission costs and shorter development time compared to larger space-based missions (Serjeant *et al.* 2020). This is promising for making space-based astronomical observations accessible to universities and research institutions alike. Additionally, CubeSats may also be used as a platform for technology demonstration and space qualification of critical components and systems, and hence serve as a testing platform for bigger astronomical missions (Morgan *et al.* 2019). However, implementations based on CubeSats have to navigate around the following practical issues:

- *Pointing stability limitations:* Astronomical telescopes typically require arcsecond-level pointing

accuracy in the line-of-sight direction and must maintain this pointing with minimal deviation for the complete duration of observation. Space-borne astronomical telescopes must achieve this while in the presence of various sources of micro-vibrations, such as disturbances resulting from magnetic torques, solar radiation pressure, gravity gradient torques, and several other factors (Paluszek 2023). Conventional Attitude Determination and Control Systems (ADCS) are typically designed for larger platforms with higher mass (and hence inertia) ratios between the reaction wheel and the platform and are not sufficient for arcsecond-level attitude stabilisation on CubeSat-type platforms (Douglas *et al.* 2021). Typically, a separate finer control loop is required to correct for the disturbance from within the optical chain of the telescope itself (Peri *et al.* 2023).

- *Limited aperture and focal lengths:* The CubeSat specification defines the exact envelopes within which the complete spacecraft (including the telescope, instruments, and avionics) must fit.[1] Typically, the largest of CubeSats allow for 12U volume in 2UX2UX3U format, where 1U is typically considered a cube with sides of 10 cm. The largest symmetrical telescope aperture that can fit within this volume is about 200 mm in diameter (about 185–190 mm might be more realistic). On smaller CubeSats, e.g., 6U (1UX2UX3U), a 100 mm aperture is more typical. There have been some attempts to maximise the available collecting area, such as by using a rectangular aperture (e.g., CUTE, Fleming *et al.* 2017) or an off-axis primary mirror (e.g., CUBESPEC, Raskin *et al.* 2022). This restriction in aperture highlights the necessity of being efficient with the gathered photons and being creative with the science programs.

CubeSat-based platforms have the potential to be diffraction-limited. However, the smaller aperture and limited space envelope also limit the focal length of CubeSat-based telescopes. Invariably, this leads to a fairly high plate-scale (of the order of hundreds of arcsec/per mm) at the image plane; and fairly small pixel size (about 2–4 microns) is required to adequately sample this PSF. Detectors arrays with such small pixels are typically not aimed for scientific observation and therefore (depending on the nature of the science

being attempted) might need dedicated facilities for their characterisation before launch. At the same time, the use of a larger pixel size will cause the PSF to be undersampled.

- *Size, complexity and reliability:* Although smaller in size, CubeSats must operate in a self-sufficient manner in terms of power, communication, onboard computing, battery backup, coarse pointing, and other miscellaneous subsystems. Fortunately, there have been significant efforts from commercial companies[2,3] towards the availability of standardised CubeSat buses. Similarly, progress is being made towards miniaturizing mission-critical components, such as reaction wheels, magneto-torquers, and star sensors (Johnston-Lemke *et al.* 2011; Candini *et al.* 2012). Still, the complexity of CubeSats (that are capable of useful astronomy) remains a challenge and will probably benefit from further standardisation of components and systems as well as collaborative work between the astronomical community and the industry.

Keeping these aspects in mind, we introduce a framework of astronomical telescopes based on on-axis afocal optics. The general design considerations are aimed at suitability for use in a compact CubeSat platform. We discuss the advantages and flexibility of such a framework along with several example designs and some illustrative science cases.
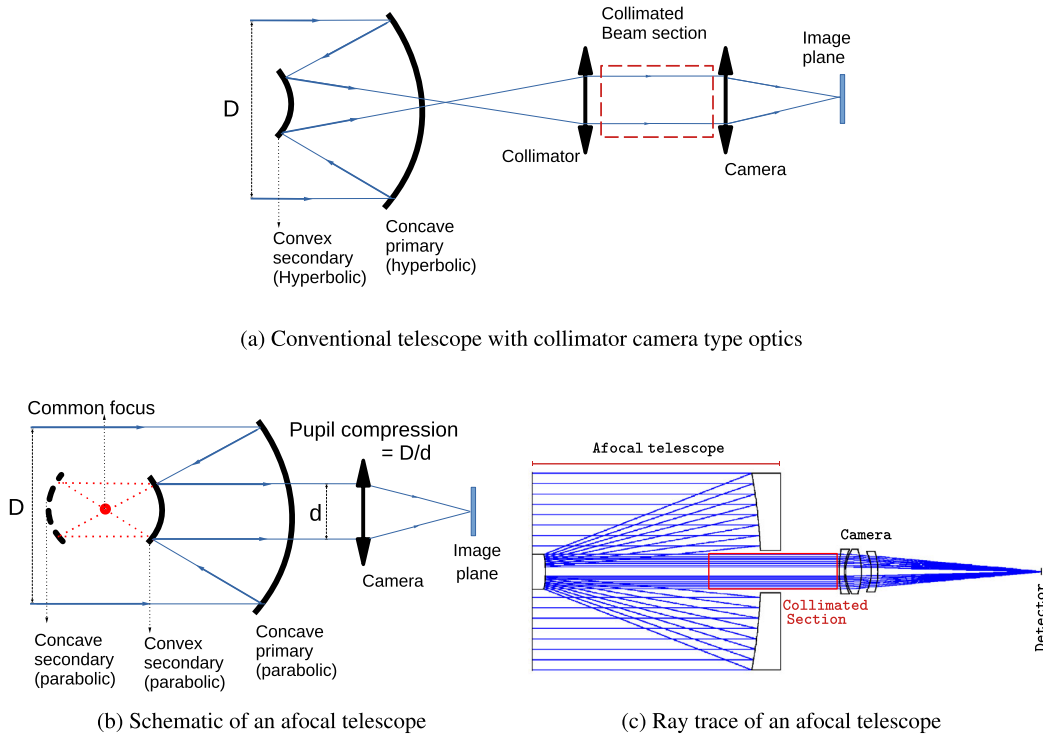
2. General principle of afocal telescopes

Afocal optical systems are defined as those systems that do not have a finite focal length associated with them. These typically have zero power and need a minimum of two optical components to be implemented (Hazra 2022). Practical examples of such systems include laser beam expanders (Mahajan 1998) and guide star launchers for adaptive optics (Clermont *et al.* 2020) as well as the classical Mersenne telescope. A detailed analysis of aberrations cancelling properties of the afocal telescope is presented in Baker (1969), and a few more examples can be found in Terebizh (2019). In recent times, the COROT mission used an off-axis afocal telescope (Auvergne *et al.* 2009).

In modern astronomy, there is often a need for a collimated beam section to accommodate gratings,

---

[1] https://www.cubesat.org/.

[2] https://www.bluecanyontech.com/.

[3] https://hex20.in/.

(a) Conventional telescope with collimator camera type optics

(b) Schematic of an afocal telescope

(c) Ray trace of an afocal telescope

Figure 1. Layout of an afocal telescope with a camera: an afocal system in (b) is compared to a conventional design in (a). In the case of the conventional design, the telescope produces a real image at the Cassegrain focus. This image may be recollimated by a collimator optics and then reimaged by a camera optics. The collimated beam section is used to place filters, GRISMS, etc. However, for the afocal telescope shown in (b), the combination of primary and secondary produces a collimated beam output that is only pupil compressed. This collimated beam is immediately available for placing components, such as filters, GRISMS, or for the purpose of beam steering. The final telescope F-number and platescale are determined by the camera optics. In (c), a real ray trace of an afocal system is shown to highlight the compactness of the system.

GRISMs, filters, or polarisation components. Typically, a collimated beam section is made available by means of a collimator, camera-type optics, such as in Figure 1(a). However, an alternate method to produce a collimated beam section is shown in Figure 1(b) by means of an afocal system realised by means of two confocal paraboloids. A paraboloid has two conjugate points between which it achieves aberration-free imaging. One of these points is at the focus of the parabola, while the other point is at infinity. The primary mirror images the star (located at infinite object distance) onto its focus. However, this point is also the common focus for the secondary mirror. Therefore, the secondary mirror re-images the focus to its other conjugate point, which is at infinity. The output is a collimated beam that has been pupil compressed. The ratio of compression can be expressed as:

$$C = \frac{D}{d} = \frac{F_p}{F_s}, \tag{1}$$

where D and d are the diameters of the primary and secondary mirrors, respectively, and F_p and F_s are the focal lengths of the primary and secondary mirrors, respectively. Since confocal parabolas satisfy the on-axis conjugate imaging condition, the beam compression is aberration-free for the central field. In later sections, we demonstrate that it is possible to achieve good imaging performance to about 20–30 arcmin in these types of systems.

A camera is needed after the afocal telescope as shown in Figure 1(c). The effective focal length of the complete system, as well as the field-of-view (FOV), is related to that of the camera by:

$$F_{\text{telescope}} = C \times F_{\text{camera}} \tag{2}$$

and

$$\text{FOV}_{\text{telescope}} = \frac{\text{FOV}_{\text{camera}}}{C}, \tag{3}$$

where $\text{FOV}_{\text{camera}}$ is the 'apparent' FOV of the camera optics. The camera optics work at a smaller aperture, where more flexibility is available. If required, strongly aspheric and free-form optics may be utilised. The afocal telescope is primarily responsible for providing a

beam compression; the final image quality and plate-scale are largely dependent on the camera optics. It creates a unique opportunity to standardise the primary and secondary mirrors across a range of output F-numbers and wavelength ranges. Several illustrative examples are presented in later sub-sections 4.1 and 4.2.

Limitations of afocal designs

The afocal design is not necessarily the most compact implementation possible. Depending on specific output F-numbers required (typically for fairly short F-numbers – <F6), it is possible to realise catadioptric systems that are shorter than afocal systems. One such example is shown later (sub-section 4.1). For longer focal lengths, the afocal design is usually a fairly compact implementation.

   Compared to the collimator-camera type implementation, the afocal design does not have an exit pupil in an accessible place. For a convex parabolic secondary, the exit pupil is actually formed behind the secondary mirror and is not accessible. Off-axis designs using a concave secondary can bring this exit pupil to a more accessible spot (e.g., COROT, Auvergne *et al.* 2009). However, this implementation is difficult to scale down to the permissible volumes of a CubeSat. Similarly, since there is no intermediate focus, there is also no place to include a slit, and therefore, the present work focuses only on imagers and slit-less spectrographs.

Advantages of afocal designs

- *Standardised testing and characterisation:* Same primary and secondary can be used across a range of different types of instruments; thus simplifying the process of testing and characterisation.
- *Flexibility in the choice of detector:* The final platescale is only determined by the camera, which can be optimised for a specific detector in mind, while keeping the primary and secondary mirror configuration fixed. This allows for the use of off-the-shelf or commercial detector modules whenever possible.
- *Lower part count and SNR advantage:* By eliminating the collimator group from a standard layout, the part count is reduced, and thereby a simpler and higher throughput system may be realised.
- *Ease of fine steering and pointing stability:* A unique advantage of the afocal design is the immediate availability of the collimated beam section. Beam steering from within a collimated

beam section has significant advantages (discussed in the next section) and allows for simpler implementations of fine steering control loops.
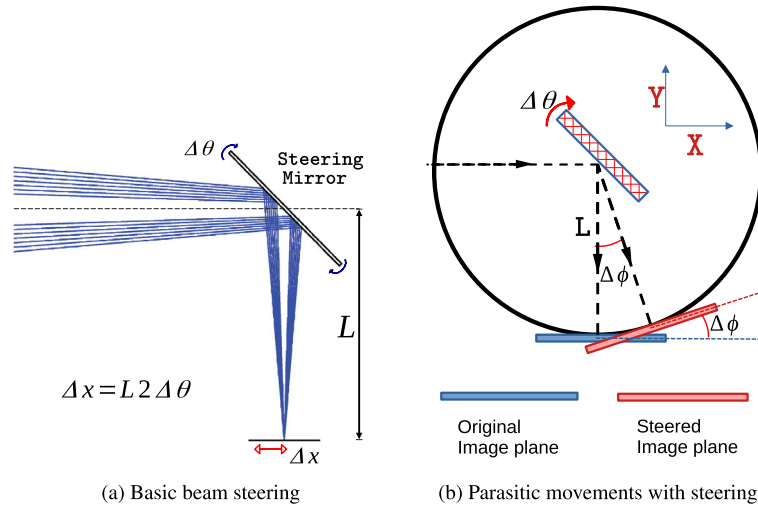
3. Beam-steering for fine pointing stability

Astronomical telescopes require line-of-sight pointing accuracy at arcsecond levels or better. Although it is possible for some larger observatories to make use of reaction wheels and magneto-torquers to achieve high line of sight stability (e.g., Hubble, Beals *et al.* 1988 and COROT, Auvergne *et al.* 2009), this is much more difficult for smaller spacecraft, such as those based on CubeSat formats. This is partly due to the presence of more micro-disturbances in the low Earth orbits typical of CubeSats as well as an unfavourable ratio of typical reaction wheel mass to the spacecraft inertia (Douglas *et al.* 2021). There have been efforts to miniaturise reaction wheels for CubeSat applications (e.g., Johnston-Lemke *et al.* 2011); and commercial CubeSat buses nowadays advertise stability of about an arcmin or even less.[4] Still, this by itself is not sufficient for astronomical applications.

   For astronomical usage of CubeSats, it is necessary to implement a separate fine control loop (e.g., in the CUBESPEC mission, Peri *et al.* 2023) in addition to the spacecraft's pointing control. This loop is implemented by fine guidance sensors that can sense the deviation in pointing direction at a high enough resolution, and a beam steering mechanism to correct for the deviation. The fine guidance sensor can be realised either using a fibre optic gyroscope (Sanders *et al.* 2012; Jin *et al.* 2018) or a fine guiding camera (Rowlands *et al.* 2004). Due to space constraints of the CubeSat-type platforms, we will focus mostly on the fine guiding camera. The guiding information is utilised by a fine steering mechanism to correct for pointing error. The different mechanisms for the same can be classified into three broad categories (for a more comprehensive review of different actuators and mechanisms, Milaševičius & Mačiulis 2023 is a good source):

- *Micro-thrusters:* Precise amount of correcting torque can be applied to the complete spacecraft using micro-thrusters (Mandić *et al.* 2018; Flinois *et al.* 2022). A practical example of this is the Euclid observatory (Mellier *et al.* 2024). This approach may hold promise for CubeSats in the future (Levchenko *et al.* 2018; Dennehy *et al.*

---

[4]https://www.bluecanyontech.com/.

(a) Basic beam steering

(b) Parasitic movements with steering

Figure 2. Beam steering with a flat mirror: The basic principle of beam steering with a flat mirror is shown in (a). Angular motion of the steering mirror produces a 'linear' displacement of the image at the image plane. This motion is amplified by having the image plane at a larger distance from the steering mirror. For small steering angles, the motion at the image plane can be approximated as a linear translation of the PSF. However, at larger angles, the parasitic motions are non-negligible. The general case is shown in (b). The beam steering in this case is along a circle centred around the mirror centre. In this case, a larger steering circle is preferable.

2020), but at present is limited by the extra weight of fuel and limited lifetime.

- *X-Y stage at the detector plane:* Let us consider a telescope of focal length F, if there is a pointing inaccuracy of $\Delta\alpha$ (in arcsec units), the corresponding image motion at the detector plane is:

$$\Delta x = \frac{F\Delta\alpha}{206265}, \tag{4}$$

(the factor 206265 can be omitted if $\Delta\alpha$ is expressed in radians) This error can be cancelled by translating the detector via an X-Y stage. This method was attempted for both the PICSAT (Nowak *et al.* 2016) and ASTERIA missions. The ASTERIA mission (Pong 2018) has successfully demonstrated that this principle is capable of achieving arcsecond-level accuracy. The typical piezo-driven X-Y stages used in this method have a range limitation (<1 mm), so they are typically suitable for short focal length imagers.

- *Fine steering mirror:* The motion required at the detector plane is higher as longer focal length systems are to be accommodated or bigger errors are to be corrected. In such cases, fine steering mirrors are a general-purpose solution for beam steering as they can accommodate spectrographs as well as basic imagers. The steering mirror acts as a lever and amplifies the motion. The basic principle is shown in Figure 2(a). The translation

ΔX at the image plane is given by:

$$\Delta X = \frac{2L\Delta\theta}{206265}, \tag{5}$$

where L is the steering distance and $\Delta\theta$ is the steering angle (again expressed in arcsec) of the mirror from its nominal position. To correct for the pointing drift, the steering motion must be equal to its magnitude and opposite in direction; therefore:

$$\Delta x = -\Delta X.$$

The negative sign may be ignored if one is only concerned about the magnitude of the steering angle, which can be rewritten as:

$$\Delta\theta = \frac{F\Delta\alpha}{2L}. \tag{6}$$

This method is used in JWST, Ostaszewski & Vermeer (2007), Herschel (SPIRE instrument, Pain *et al.* 2003), as well as for the planned mission CUBESPEC, De Maeyer *et al.* (2024), as well as a number of satellite communication missions.

3.1 *Aberrations arising from beam steering*

An ideal beam steering solution is one that allows for controlled, large-amplitude motion in the image plane without degrading the PSF. However, X-Y stage or

FSM-based steering modifies the optical layout in some manner and hence introduces steering-related aberrations. For an X-Y stage, this aberration is mostly due to small deviations within the beam path as the pointing direction 'wanders'. This can be reduced by over-sizing the optics and optimising for a larger FOV than is imaged onto the detector. For example, let us consider a camera that images 10 arcmin onto a detector. If the expected coarse pointing stability is 2($\pm$1) arcmin, then the optics must be designed for 12 arcmin.

FSM-based beam steering is more complex, as significant additional aberrations are introduced by the steering mirror. When a converging beam is steered by a flat mirror, the optical path length is conserved along a circle (Figure 2b). Therefore, beam steering (in 2 dimensions) by a flat mirror produces the best image on a sphere rather than a flat surface (Bagnasco *et al.* 2007). The centre of the sphere is coincident with the steering mirror. In reference to the detector, this produces three separate motions. The first motion is along the X-axis, expressed as:

$$\Delta X = 2L\Delta\theta \times \cos\Delta\phi. \tag{7}$$

This is the desired steering motion and simplifies to Equation (5) when $\Delta\phi$ is small. The second is a defocus along the Y-axis expressed as:

$$\Delta Y = 2L\Delta\theta \times \sin\Delta\phi. \tag{8}$$

This defocus can be made small by keeping the steering angle small. The third motion is an out-of-plane rotation in the image plane,

$$\Delta\phi = 2\Delta\theta. \tag{9}$$

This produces a defocus at different field points of the image plane. Particularly, the defocus is positive for one half of the image and negative in the other half. The maximum defocus scales with the size of the image plane and can be written as:

$$\Delta Y' = \pm\frac{W\Delta\phi}{2}, \tag{10}$$

where W is the size of the image plane.

JWST deals with the steering-related aberrations by matching the field curvature of the intermediate telescope focus to that of the steering sphere (Bagnasco *et al.* 2007). This method can not be scaled down to CubeSats, where available space is very limited.

One additional source of image degradation arises from off-centre steering of the FSM. Typically, steering actuators are placed behind the mirror. The steering axis of the mirror is offset from the optical surface by a distance equal to the substrate thickness D. A corresponding defocus of:

$$\Delta Y = 2D\sin(\Delta\theta), \tag{11}$$

is seen at all field points of the image plane.

A comparative simulation of three separate steering arrangements is presented in Figure 3(a). In the first two arrangements, steering is done in an F10 converging beam with a steering distance of 225 and 50 mm, respectively. The third arrangement steers the beam in a collimated beam section, followed by an F10 camera.

In the case of beam steering in a collimated beam, the motion at the image plane can be expressed as:

$$\Delta X = 2f_a\Delta\theta, \tag{12}$$

where f_a is the focal length of the imaging assembly following the steering mirror.

In all three systems, the output is steered by tilting the steering mirror from its nominal position. The RMS spot radius is recorded for a number of different fields for each incremental tilt of the steering mirror. The degradation of the RMS spot radius is shown in Figure 3(b). It is evident that degradation is inversely proportional to the steering distance. The major contributor to such degradation is the out-of-plane rotation of the image plane, which introduces a positive defocus on half of the image plane and a negative defocus for the other half. In the case of the shortest beam steering distance, the out-of-plane rotation of the image plane is significant enough to be visible near the focal plane (Figure 3c). It makes sense to allow for a large L to minimise the degradation of the spot. In this aspect, the afocal system has a particular advantage; since from the perspective of the imaging system, the object is at infinity, the optical distance between the image plane and the steering mirror can also be considered infinite. Therefore, a reasonably well-optimised system is expected to show little or no degradation by beam steering from within a collimated beam section.

The spot degradations arising from this defocus are shown in Figure 4(b). Since defocus is uniform across the field of view, data is plotted only for one field. Once again, it is seen that setting the steering distance very short introduces the most RMS spot degradation. This is related to Equation (5), since the steering distance L is small, a larger steering angle $\Delta\theta$ is required, and hence a larger amount of defocus is observed. The afocal system shows no degradation in this scenario; this is expected since small amounts of defocus in a collimated beam introduce no change in the image location.
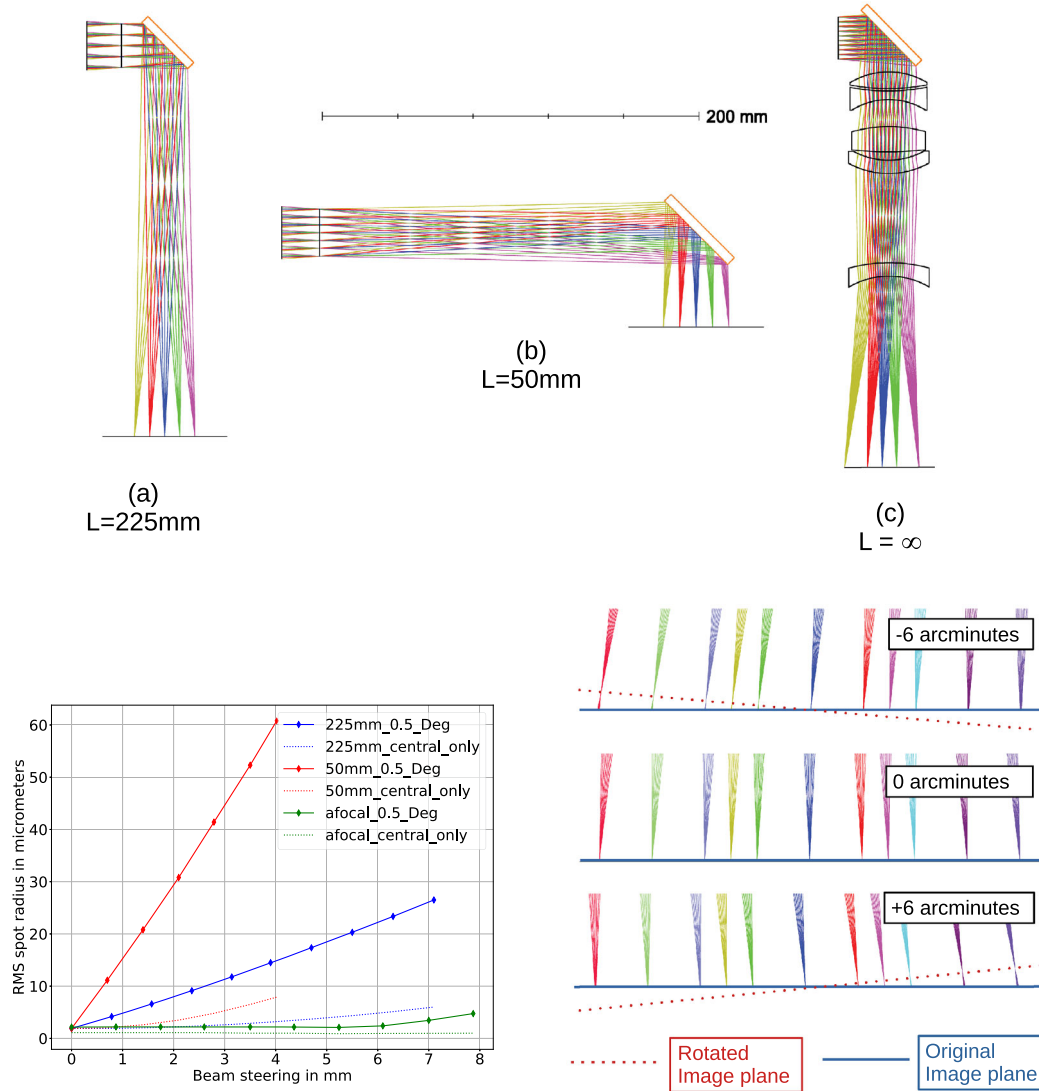
Figure 3. Comparison of efficacy of different steering mechanisms: layout of three different steering arrangements is shown in (a). The first two steer the beam in a converging beam at 225 and 50 mm from the image plane, respectively. In the third one, the beam is steered in a collimated section. All three systems have the same output (F10) and a similar aperture. The degradation of the RMS spot vs. steering angle is shown in (b). Steering from a shorter distance produces a tighter steering circle and hence significantly more degradation. The primary source of this degradation is an out-of-plane rotation of the image plane illustrated in (c). Steering in the collimated beam section produces the least amount of degradation.

We have presented a general description of the complexities related to beam steering by means of an FSM. The results are summarised as follows:

- The degradation is inversely proportional to the steering distance – distance from the image plane to the centre of the steering mirror.
- The degradation is directly proportional to the physical size of the image plane.
- A defocus proportional to the thickness of the steering mirror is also seen.
- Beam steering within a collimated beam section avoids these aberrations.

We have highlighted that beam steering within a collimated beam section has inherent advantages. Afocal telescopes conveniently produce a collimated section without the need for extra collimator optics. As such, afocal designs are a natural fit for CubeSat-based observatories looking to utilise FSM-based pointing stabilisation.
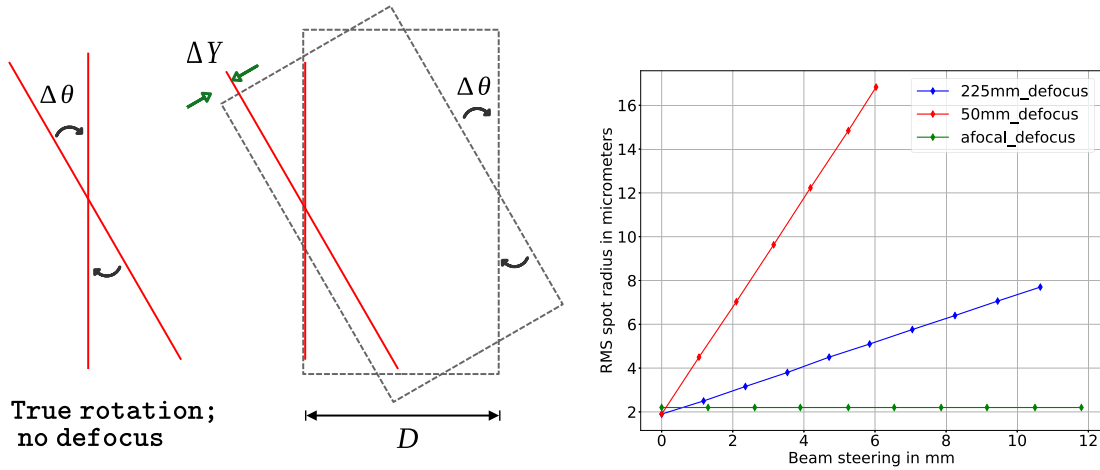
Figure 4. Defocus by rotation of a real steering mirror: If a mirror is rotated about a centre that is not coincident with the reflective surface, an angle-dependent defocus will occur, as shown in (a). The extent of this defocus depends on the steering angle and the thickness of the mirror. The required steering angle is also larger in the case of a smaller steering circle. The spot degradation at the image plane is shown in (b) for a mirror thickness of 5 mm. The plot shows the amount of image defocus for the same amount of linear steering at the image plane. The effect of longer steering distance is obvious, and it is also seen that beam steering from within a collimated section is largely unaffected by offset in the rotation axis of the mirror.

4. CubeSat-based observatory templates

A complete observatory must include some provision for coarse and fine guiding as well as beam steering mechanisms to provide a stable image at the focal plane for long integration durations. It must also include necessary avionics components, such as battery, computation, reaction wheels, magneto-toque, communication antennae, etc. It is desirable to have a significant number of components/subsystems to be standardised and realised using modular and off-the-shelf components. This approach reduces cost, effort, and the time for practical implementation as well as testing and characterisation of components. However, we also desire that our observatory framework be flexible enough to target specific science cases. We present an optical framework based on afocal designs to accommodate both of these goals. We present two design templates based on standard 12U CubeSat geometry. One template uses four instances of 10 cm aperture telescopes, and the other uses a single 20 cm aperture telescope. We demonstrate that it is possible to realise a range of scientifically relevant designs using the same off-the-shelf primary mirror. The secondary mirror is also kept identical across all afocal designs within a template. The optomechanical design of the afocal telescope is very similar to a conventional RC-type telescope. Therefore, the telescope as the 'light gathering element' can be standardised. The final output parameters, such as F-number, wavelength range, and field of view, are mostly

decided by the camera optics. Optical design of several such cameras, along with relevant science cases, is discussed. Also, both of these templates allow for some provision for a fine guiding camera (although in slightly different manners) and leave ample space for the avionics components and other vital subsystems. To allow for complete and reliable avionics components, a minimum of 4U volume (about 4000 cm^3) must be allocated for the avionics components. Therefore, the optics must fit within an 8U volume. The templates are discussed below.

4.1 *Observatory template using 1U aperture telescopes*

A schematic plan for implementing a CubeSat-based observatory from 1U aperture telescopes is shown in Figure 5. The complete system is to be implemented in a standard 12U CubeSat. The official 12U standard is somewhat larger than the 2UX2UX3U format and is allowed to be of size 226 × 226 × 366 mm. The template follows this size guideline.[5] Figure 5(a) shows the top view, which describes the allocation of available aperture towards guiding and science instruments. Similarly, Figures 5(b) and 5(c) illustrate the space allocated for science instruments and for avionics. The complete aperture is divided into a total of 5 sub-apertures. Two of these apertures are reserved for coarse and fine guiding;

---

[5]https://www.cubesat.org/.

(a) Top view   (b) Side view

(c) Side view
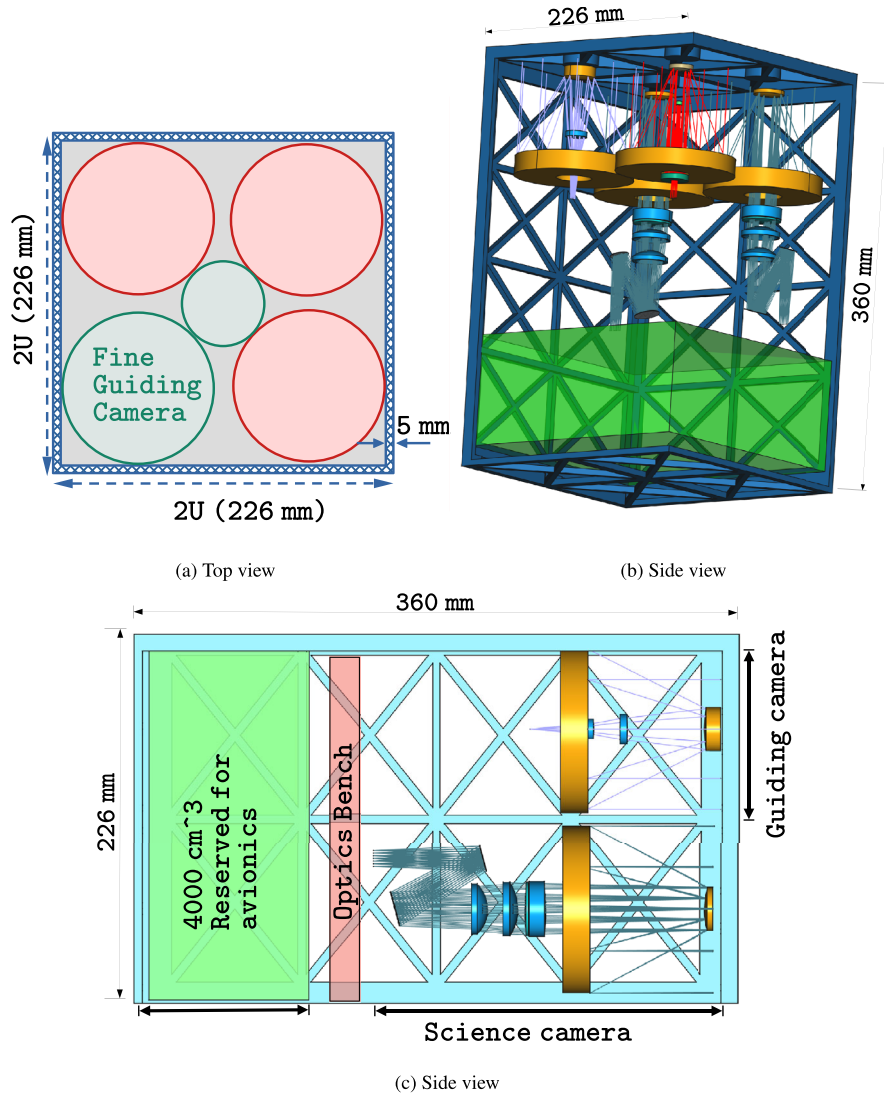
Figure 5. Plan for a CubeSat observatory utilising four separate 10 cm aperture telescopes. The entire observatory fits within a 12U volume, of which about 6–8U is reserved for the optical telescope and components. The aperture distribution is shown in (a). The space allocation within the 12U volume is shown in (b) and (c). Suitable fine guiding cameras for this template are shown in Figure 6, and science-focused optical designs are shown in Figures 8 and 9.

the remaining three apertures are for science-focused instruments. Out of the three available science apertures, two can be made into a 1U X 2U volume, while the other one can be only a 1U by 1U to allow for some space for avionic components. The monolithic camera, as in Figure 6(a), is a good match for the 1U camera.

The coarse guiding aperture is allocated to a star-sensor (similar to ones already developed and space qualified at IIA, Chandra *et al.* 2024a). This camera, working in tandem with the spacecraft Attitude Determination and Control System (ADCS) module, must provide initial pointing stability within 2–3 arcmin. The fine pointing stability is provided by a closed-loop control involving a 1U aperture fine guiding camera and

individual X-Y translation stages on all apertures. As discussed earlier (Section 3), X-Y stage actuators work well for optical designs that have fairly short focal lengths. A number of suitable X-Y stages are shown in Table 2 corresponding to different focal lengths of the cameras. It is of note that if the required precision is met, then a longer travel stage may be used for a shorter focal length, but not vice versa. The fine guiding is to be provided by a 1U guiding camera. Two competing designs are shown in Figure 6; one of them uses an afocal telescope followed by a monolithic camera, the other uses a catadioptric system consisting of an RC telescope and three lens elements. Both of these designs use the same off-the-shelf primary mirror and are intended for
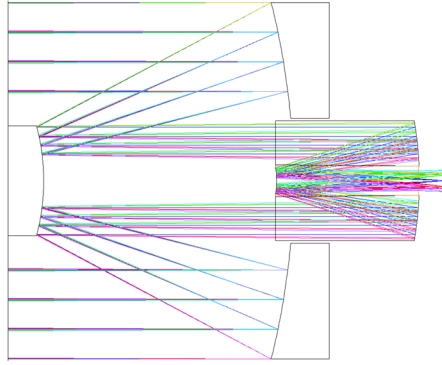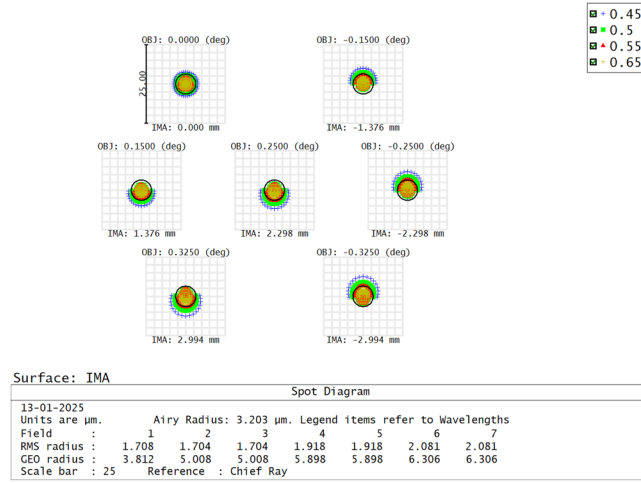
(a) 1U monolithic guider
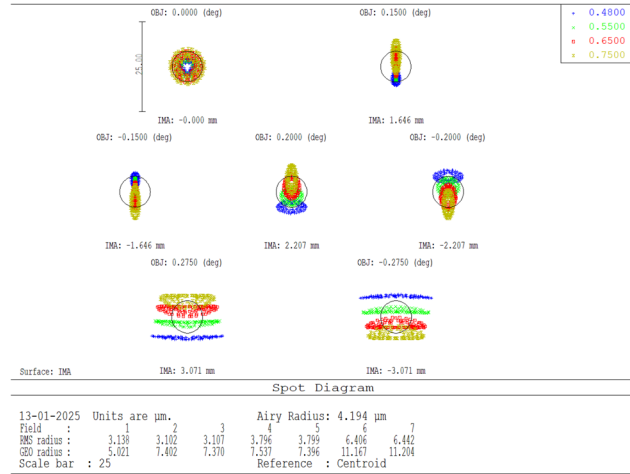
(b) Spot for monolithic guider
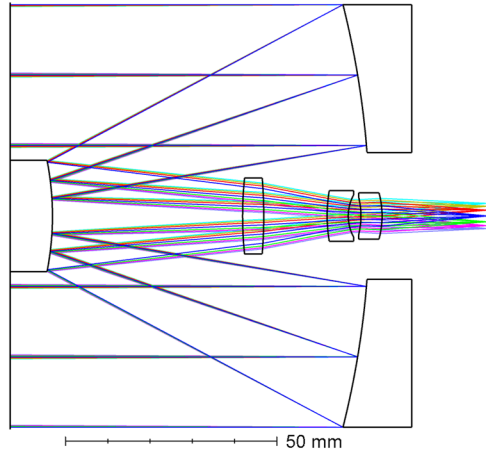
(c) 1U Guider using 3 lens elements

(d) Spot for 1U guider

Figure 6. Comparison of two guide camera designs: the layout in (a) is by means of a monolithic camera following an afocal telescope. This design has an output of F6.25 and a field of view of about 30 arcmin. The corresponding image performance is shown in (b). Similarly, the layout of a 3-lens corrector following a fast telescope is shown in (c). This design has an F5.25 output and is optimised for a field of 40 arcmin. The imaging performance is shown in (d). The 3-lens catadioptric system is marginally better in terms of field of view and image quality.

use with the IMX477 sensor from SONY. The monolithic telescope is optimised for a field of view of 30 by 22.5 arcmin and at an output of F6.5 produces 0.49 arcsec per pixel on the 1.55 micron pixel of IMX477. The 3 lens catadioptric system is optimised for 40 by 30 arcmin and produces an F5.25 output and 0.6 arcsec on the same detector. The pixelscale is an important parameter, as this largely defines the fine guiding resolution of these cameras. Comparing the performance of both of these designs, it is seen that the monolithic guider falls marginally short in terms of image quality compared to the 3-lens design. The sensitivity limits of both of these designs in the V band (closely approxi-

mated by the G filter of the Bayer pattern) is shown in Figure 7 and the probability of finding a guide star is listed in Table 1 illustrating that these designs are fairly suitable as 'all-sky' guiding cameras.

*1U template: Afocal design examples*

A number of optical designs are presented to illustrate the versatility and flexibility of the afocal template. A few refractive camera designs are shown in Figure 8, and fully reflective camera designs are shown in Figure 9. All the designs presented are of the same outline; an afocal telescope is followed by a suitable camera. The

afocal telescope (i.e., the combination of the primary and secondary) itself is fixed across all the designs. Further, the primary mirror is actually an off-the-shelf (from Optisurf[6]) 10 cm aperture F1 primary mirror, which is chosen for its fast output to save space.

Whenever possible, each optical design is also paired with a tentative detector. A list of useful small form factor detectors is listed in Table 3. In particular, several sCMOS-type detectors from SONY are highlighted. A few of these have interesting wavelength coverages, such as IMX487 in NUV and IMX990 in NIR (Smilo *et al.* 2024). Additionally, larger arrays of the same family have been evaluated for scientific use and have been known for relatively low read and dark noise and acceptable uniformity across the sensor (Alarcon *et al.* 2023; Betoule *et al.* 2023). Typically, these arrays achieve better than $0.1 \, e^- \, S^{-1}$ in dark current for modest cooling requirements (about 5°C). Modern CMOS readout circuits are also fairly compact[7] and are based on standardised interfaces, such as SLVS-EC[8] which directly connect the detector to an FPGA or controller. A flexible PCB[9] is particularly useful as the interface allowing for freedom in detector mount and operation.

Similarly, a number of compact MCPs and suitable CCD/CMOS sensors are also included in the table for the NUV and FUV wavelength range. These MCPs are fairly compact and can be paired with compact high-voltage power supplies (e.g., C10940 and C11152 from Hamamatsu). There has been progress on readout of MCPs by using simple Raspberry Pi-based cameras at IIA (Chandra *et al.* 2024b). However, MCPs typically have low quantum efficiency, and one may consider replacing them with some modern CCD/CMOS-type detectors for certain wavelength regions. The short wavelength limit of these detectors is typically decided by the window material. Hamamatsu offers some of the CCDs without a window,[10] and can achieve close to 30–40% efficiency at 130 nm and about 60–70% at 150 nm.

The design in Figure 8(a) is a visible camera. The design is based on a 3-lens system. The output is F7 and is fairly well optimised for a field of view of 30 arcmin and a wavelength range of 450–800 nm. The primary use

Guiding limits v stellar distribution
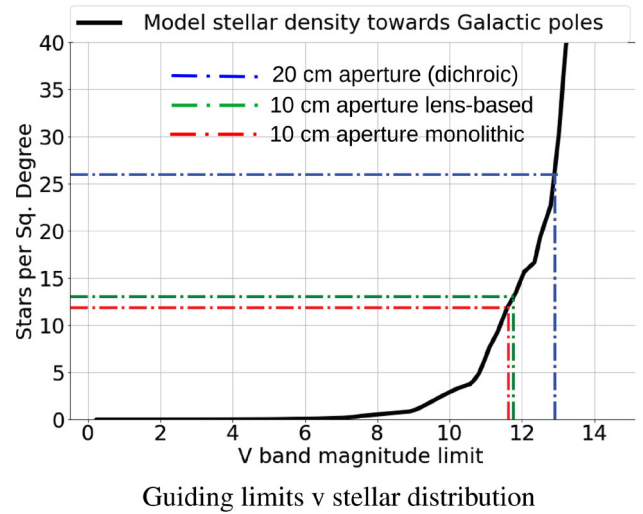
Figure 7. A comparison of guiding limits of various cameras: the SNR limits for guiding cameras is plotted along with model stellar distribution from Douglas *et al.* (2021). The green and red line are for 1U guiders (monolithic and lens based, respectively) in Figure 6, and the blue line is for the 2U guider shown in Figure 13. The corresponding stellar density in terms of stars per square degree is used to estimate the probability of finding at least one star in the field of view (Table 1).

of such a camera would be as a general-purpose wide-field camera. The output matches well with sensors, such as IMX477[11] or IMX226. A nominal pixel scale of 0.45 arcsec per pixel is achieved for the IMX477 sensor. The spot diagram of this design is shown in Figure 8(b). This design is optimised to be close to the diffraction limit for the entire field of view as well as the full wavelength range of sensitivity.

Similarly, in Figure 8(c), an NIR imager is presented. This NIR imager is designed with an InGaAs sensor, such as SONY-IMX992, in mind. This detector has a pixel size of 3.45 microns and is available in formats up to 2.5K by 2K. The wavelength sensitivity range is typically from 600 to 1750 nm, while good quantum efficiency is achieved from 900 to 1700 nm. Modern InGaAs arrays are quite capable for astronomical and scientific applications (Lourie *et al.* 2020; Smilo *et al.* 2024; Yang *et al.* 2025). The outstanding feature of InGaAs arrays when compared to H2RG detectors is that InGaAs arrays typically can be operated with minimal cooling requirements. Simple Peltier cooling is often sufficient, and the weight and complexity of a cryogenic system are avoided. This makes them a simple and affordable alternative (Batty *et al.*

---

[6]https://optisurf.com/.

[7]https://www.framos.com/en/products/sony-imx541aamj-evb-kit-slvs-ec-c-mount-24063.

[8]https://www.sony-semicon.com/en/technology/is/slvsec.html.

[9]https://www.qhyccd.com/qhy-space-camera-series/.

[10]https://www.hamamatsu.com/content/dam/hamamatsu-photonics/sites/documents/99_SALES_LIBRARY/ssd/uv_koth0022e.pdf.

[11]www.raspberrypi.com/products/raspberry-pi-high-quality-camera/

Table 1. Three different guiding cameras are evaluated, the field of view as well as limiting magnitudes for 0.5 s exposure (SNR = 10) is presented. The quantity P is the probability of finding at least one guide star within the field of view. This probability is calculated for stellar density models toward the Galactic poles (Figure 7) and hence is a conservative lower bound.

Design	FOV	Pixelscale	V_{mag}	P
1U (lens)	$40' \times 30'$	$0.6''$	11.62	0.97
1U (mono)	$30' \times 22'$	$0.5''$	11.76	0.92
2U (lens)	$21' \times 15.7'$	$0.35''$	12.9	0.91

Table 2. Commercial piezo-driven X-Y stages for fine steering of 1U telescopes, required range and precision are listed for an initial (coarse) pointing stability of 150 arcsec and desired stability of 0.25 arcsec.

F#	Range (mm)	Accuracy (μm)	Model
F5	0.36	0.6	Cedrat XY500M
F8	0.58	0.96	PI P-625.2CL
F12	0.87	1.5	P-628.2CL
F15	1.1	1.8	Cedrat APA1500L*
F20	1.45	2.4	P-629.2CL

* APA1500L is a single actuator, at least two must be used to implement an X–Y stage.

2022). Additionally, these detectors also do not have issues, such as ghost images and saturation. Although these arrays typically have relatively higher dark current (about 10–20 e^- S^{-1} at about −30°C[12]), they are quite suitable for imaging and photometry applications (Mishra & Kamath 2022) of brighter sources. The optical design for a 1U NIR imager is implemented in a similar fashion as the visible imager; however, the pixel size of IMX992 requires an output of F9. The layout and spot diagram are shown in Figures 8(c) and 8(d). The pixel scale is 0.8 arcsec, which is tuned to the diffraction limit of the 1U aperture for the NIR wavelength range. The design is optimised for a field of view of 30 arcmin and for a wavelength range of 850–1700 nm.

The design in Figure 9(a) is an all-reflective camera implemented by a classical Gregorian-type telescope. This results in a very compact layout that produces a fairly slow output of F18 while being compact enough to fit in a total volume slightly larger than 1U. This system achieves a focal length as high as 1800 mm and hence allows for the use of larger pixel size detectors. If the supports for the nested Gregorian can be hidden in the shadow of the afocal secondary, then this design is a useful general-purpose imager. Additionally, this design remains fully rotationally symmetric. This feature is particularly desirable for polarimetric instruments, and this will be briefly discussed at a later stage (Section 5). The spot diagram for this design is shown in Figure 9(b).
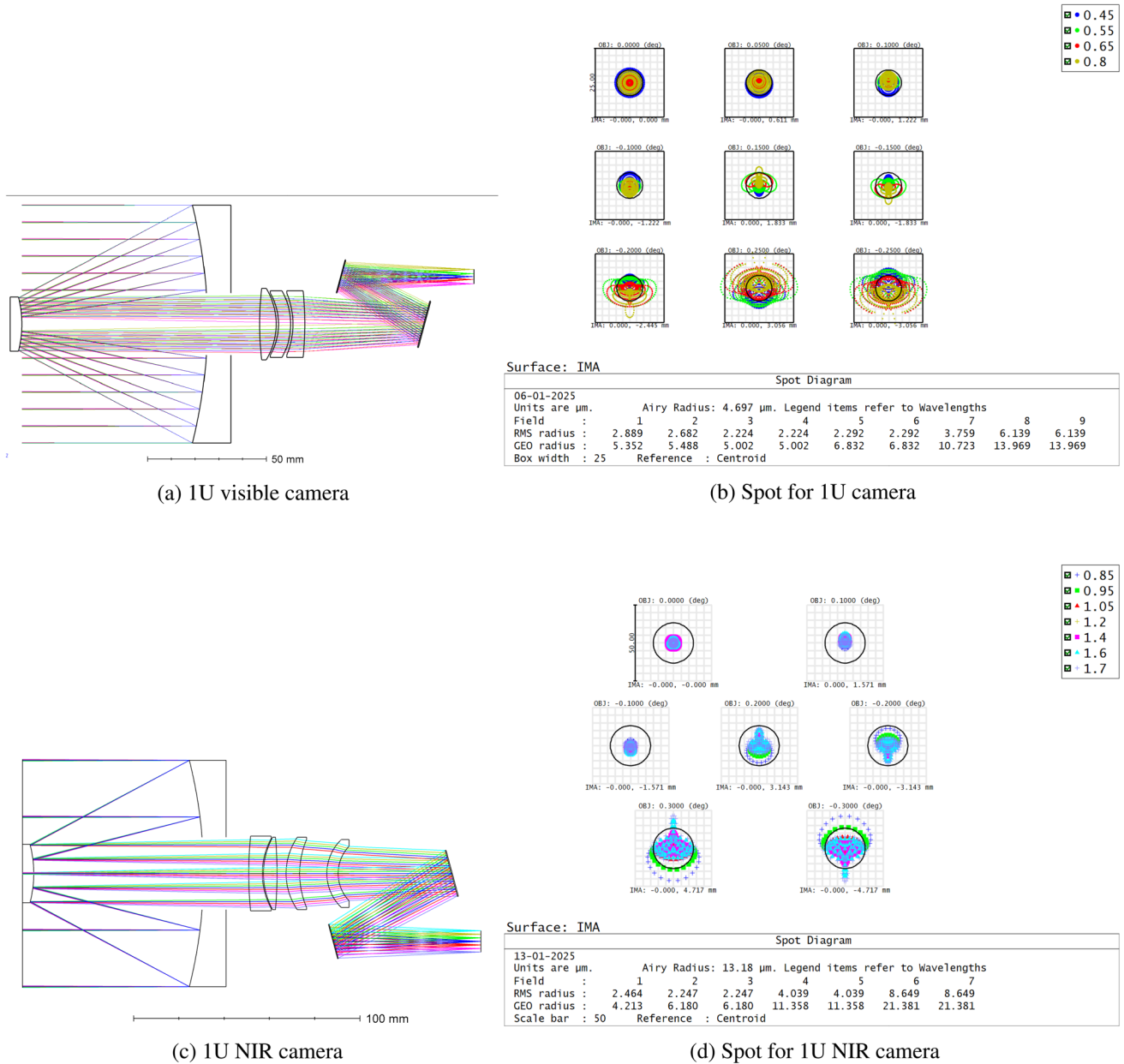
Among the designs, Figure 9(c) is particularly special as it implements the complete camera optic chain within one single piece of glass and thereby presents a unique solution. The 'monolithic telescope' as introduced by Rik Ter Horst (ter Horst & Navarro 2024) consists of a Schmidt corrector, a classical RC telescope, as well as a field flattener, all within a single block of fused silica. The version shown in Figure 9(c) (and shown in detail in Figure 10a) is a slightly simplified version without the Schmidt corrector. The exit surface that is utilised as a field flattener is also spherical. The example shown in Figure 9(c) produces an F12 output and an image size of 6.25 mm for a field of view of 18 arcmin. The combination spot diagram for the same is shown in Figure 9(d). Although the spot performance is slightly degraded from the original monolithic telescope described by ter Horst & Navarro (2024), the performance is still acceptable for the considered field of view. Additionally, since most of the optical power is generated from the reflection at the mirrored surfaces, the chromatic aberration is very small within the whole NUV-VIS-NIR range. Chromatic focal shift for the design is shown in Figure 10(b). There is some amount of field-dependent vignetting as shown in Figure 10(c). The un-vignetted fraction of rays for the central field is about 89% – the 11% drop is largely from the secondary obscuration – and it drops to about 85% for a field of about 18 arcmin. This is a particularly promising implementation of a camera in a rugged, thermally insensitive, and compact package. At present, some manufacturing concerns remain for such an unconventional design; however, the benefits of the monolithic approach are apparent for CubeSats, and correspondingly, there have been efforts to realise these designs (Smilo *et al.* 2024).

Example science case: Walraven photometry

The Walraven photometric system is a unique ground-based system that expands from visible into ultraviolet wavelength ranges. Typically, it consists of 5 photometric filters (542 nm (V), 427 nm (B), 385 nm (L),

---

[12] https://www.zwoastro.com/product/asi990mm-pro-asi991mm-pro/.

(a) 1U visible camera

(b) Spot for 1U camera

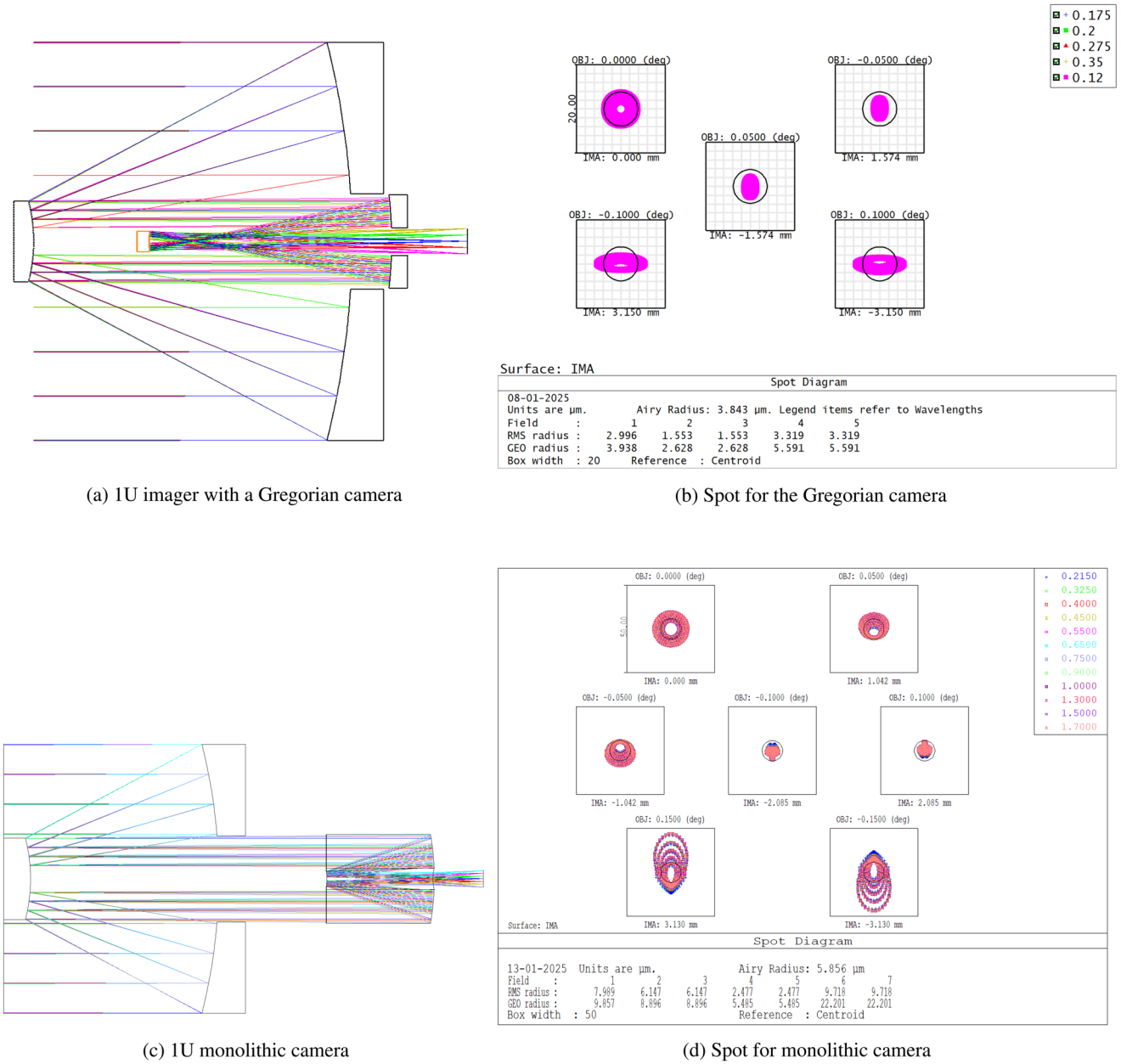(c) 1U NIR camera

(d) Spot for 1U NIR camera

Figure 8. Review of 1U designs based on dioptric cameras: (a) shows a visible camera with a fairly fast output (F7) and wide field of view. The imaging performance of this design is shown in (b), illustrating reasonably well optimised performance for up to 30 arcmin. An NIR camera is shown in (c), and the corresponding spot performance is shown in (d). The design is optimised for 30 arcmin. Both visible and NIR designs are seen to be optimised close to the diffraction limit.

362 nm (U), and 323 nm (W)). This photometric system (Walraven 1952) has been known to be excellent in determining cepheid mass and radius (Sollazzo *et al.* 1981). Colour–colour loops in U-B vs. W-U (or similar) can be a systematic as well as convenient way of determining physical parameters for pulsating variables (Onnembo *et al.* 1985). Similarly, the Baade–Wasselink method (Molinaro *et al.* 2011) in the Walraven photo-

metric system is also particularly suitable for period-luminosity and period-luminosity-colour relations. As the NUV wavelength range is particularly sensitive to pulsation-driven shocks and heating of gas, observations in this wavelength range are highly sought after. However, ground-based Walraven photometry is typically limited to fairly bright sources (3–5th magnitude) only, as atmospheric transmission is fairly poor in U

(a) 1U imager with a Gregorian camera

(b) Spot for the Gregorian camera

(c) 1U monolithic camera

(d) Spot for monolithic camera

Figure 9. Review of 1U reflective cameras: In (a), a 'nested' Gregorian camera is shown following the afocal telescope. This design can achieve fairly high F-numbers (as high as F18) and reasonable imaging performance (b) from a compact size. An example of a monolithic camera is shown in (c), and its corresponding imaging performance is shown in (d). All designs in this figure and in figure 8 use the same afocal telescope.

and W passbands. Additionally, the Walraven photometer was retired in 1991.[13] A CubeSat-based platform can extend the capability of these systems to 8–10th magnitudes. For example, limiting magnitudes for SNR 100 in Figure 11(a), along with luminosity distribution of β cepheids (Figure 11b) and classical cepheids (Figure 11c). This allows for the dedicated study of a significant number of such variables, providing an independent estimate of the mass and radius. This photometric system is also particularly suited for studying early-type stars (Van Paradijs *et al.* 1986), cataclysmic variables (Van Amerongen *et al.* 1987), as well as novae and supernovae. Magnitude distributions of some bright early-type stars are shown in Figure 16(b).

Table 3. A sample of detectors that would be suitable for CubeSat-based implementations is presented. The sensors either have relatively small pixels or a small format. The specifications of the detector, as well as some target use cases, are listed. It should be kept in mind that these are selected for the utility and opportunity they provide for a CubeSat format – particularly within the lower radiation levels of the low-earth orbit (Kimura *et al.* 2015) – and are not necessarily radiation hardened for deep space applications.

Sl. no.	Model	Manufacturer	Pixel size and format	Wavelength (nm)	Read-noise	Features and usage
1	IMX226	SONY	1.85 μm; 4 × 3 K	400–900	$3.7e^-$	VIS imager
2	IMX487	SONY	2.75 μm; 2.8 × 2.8 K	200–900	$3.7e^-$	NUV
3	IMX992	SONY	3.45 μm; 2.6 × 2 K	600–1700	$20e^-$	NIR imager
4	IMX990	SONY	3.45 μm; 1.3 × 1 K	600–1700	$20e^-$	NIR imager
5	S7170−0909	Hamamatsu	24 μm; 0.5 × 0.5 K	200–1000	$8e^-$	FUV and NUV
6	S7031−0907S	Hamamatsu	24 μm; 0.5 × 0.1 K	200–900	$8e^-$	FUV spectroscopy
7	S10141-1107S	Hamamatsu	12 μm; 2 × 0.1 K	200–1000	$4e^-$	NUV spectroscopy
8	2020BSI	GSENSE	6.5 μm; 2 × 2 K	200–900	$1.2e^-$	NUV-VIS imager
9	F1552-04	Hamamatsu	7.5 μm; 14 mm dia	–	–	MCP
10	CIS115	e2V	7 μm; 2 × 1.5 K	400–900	$5e^-$	VIS imager
11	IMX477	SONY	1.55 μm; 4 × 3 K	400–900	$\approx 3e^-$	Fine guiding
12	MT9P031	On Semi	2.22 μm; 2.5 × 1.9 K	400–900	–	Fine guiding

IMX477 is commonly available as the Raspberry PI HQ camera module.
IMX* series sensors have a different readout noise depending on the exact conversion gain used; the mentioned read noise is for high-gain count mode.

### 4.2 *Observatory template using 2U aperture telescopes*

Another conceivable template within the 12U format would be one that makes use of a single 20 cm aperture. This version has more light-gathering power allocated to one single instrument and is more suitable for observing astronomical sources in one specific manner. The available aperture for a 12U type optical system is shown in Figure 12(a). The aperture is mostly utilised by a 2U aperture telescope as well as a coarse guiding camera. All designs under this template share the same afocal telescope. The primary mirror is an off-the-shelf 20 cm aperture and F0.8 mirror from Optisurf. The telescope and scientific instrumentation are allowed to take up about 8U of the total volume, while 4U is reserved for the avionics, as illustrated in Figures 12(b) and 12(c). The fine guiding is done by dichroically splitting the telescope output into a guiding channel and a science channel (Figure 12d). A simple guiding camera for this format is shown in Figure 13. This guiding camera is also based around the Raspberry PI HQ camera module (IMX477 sensor). This camera is realised by means of 5 lens elements and produces a fast F5 output; the layout for the same is shown in Figure 13(a). The camera is optimised for a field of view of about 24 arcmin by 18 arcmin. The spot performance of this camera is shown

in Figure 13(b), and as shown in Table 1, this camera has a probability of over 0.9 to find at least one guiding star within the field-of-view. The SNR estimates are shown for 500 millisecond integrations and for fairly sparse fields (e.g., towards the Galactic poles), and hence this probability can be taken as a conservative lower bound.

The fine pointing stability is achieved by means of the Fine Steering Mirror (FSM) as shown in Figure 13(a). The FSM is responsible for correcting the pointing of both the guide camera and the science camera. It should be theoretically possible to utilise off-the-shelf tip-tilt mirrors, such as the V-931 from PI[14] or DTT10M-SG-SV from CEDRAT[15] as the FSM in this scenario. This is again made possible by the afocal implementation, which allows for beam steering from within a collimated beam section, and hence the offset rotation of the mirrors is not a significant problem; this has been illustrated in Figure 4. However, the occupied volume of these off-the-shelf modules is still a concern, and the same goes for the required electronic drivers, as well as sensor conditioning components. There is a need for miniaturization of these components as well as space-qualification and ruggedization of the complete system. In this regard, a significant amount of progress is being

---

[14] https://www.pi-usa.us/en/.

[15] https://cedrat-technologies.com/.

(a)

(b)

(c)
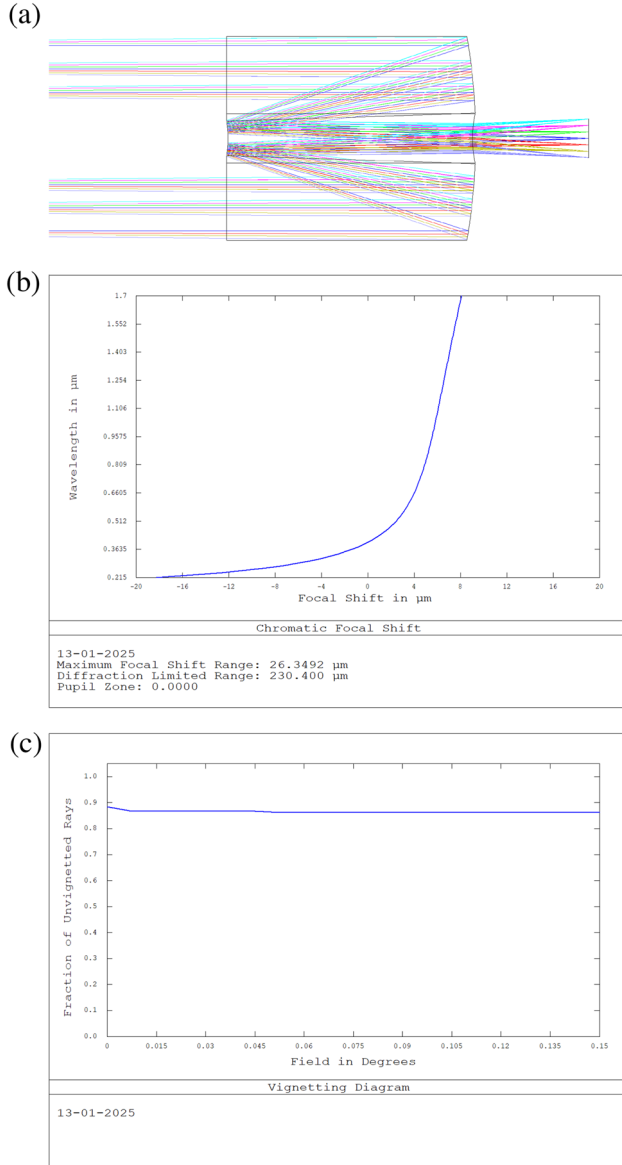
Figure 10. Monolithic cameras for afocal designs: The detailed layout of a monolithic camera is shown in (a). The camera consists of an RC telescope encased in fused silica. This camera is capable of achieving fairly large focal lengths while being fairly compact. Since most of the optical power is generated by reflection, the design is also relatively free from chromatic aberration (b), and for a well-optimised design, the field-dependent vignetting is also fairly low (c).

made, such as by De Maeyer *et al.* (2024). While there are still some challenges in terms of 'cross-talk' of rotation axes as well as deformation of mirrors under load, it is expected that a CubeSat optimised FSM will be available for the astronomical community soon.

Optical design for spectrographs utilising the 2U template is presented in Figure 14. A spectrograph focusing on the NUV wavelength range is shown in Figure

14(a). This spectrograph is implemented using a camera consisting of 3 lenses, producing an output of F9.3 and a dispersion of about 6.8 nm per mm at the image plane. The dispersion is by means of an 800 lines per mm grating (similar to models available from[16]). The spot diagram corresponding to different wavelengths is shown in Figure 14(b). The design is optimised to produce a minimum spot size along the dispersion direction, and the spot width is less than 14 microns for most wavelengths. When paired with detectors, such as S10141−1107S from Hamamatsu (Table 1), the achievable spectral resolution is about $R = 3000$ ($\Delta\lambda = 0.9$ Å) at 275 nm. An FUV spectrograph is shown in Figure 14(c). The optics for the same is based on a single off-axis mirror (the rest are flat folding mirrors). The design is intended for use in the 150–300 nm wavelength range. The design makes use of a 300 lines per mm grating and produces a dispersion of about 15.6 nm per mm at the image plane. The spot diagram corresponding to different wavelengths is shown in Figure 14(d). The resulting spectral resolution is about $R = 500$ ($\Delta\lambda = 3.6$ Å) at the wavelength of 180 nm. The spectrographs discussed above will need to be calibrated on the ground with wavelength and flux wavelengths before launch. Mercury and cadmium-based spectral lamps[17] can be used for this purpose. However, for on-orbit calibration, standard stars have to be used for wavelength calibration as well as flux calibration. In this regard, work done by Sreejith *et al.* (2022) will be quite useful. The spectrographs are intended to observe bright sources in relatively sparse fields. In case the field is more crowded, e.g., up to 2–3 stars within an arcmin, the complete CUBESAT may be rotated (along the 'roll' or line of sight axis) to position the dispersion axis along the least crowded direction of the field.

An analysis from first principles can be done to evaluate the relation between pointing stability and achievable resolution. The resolution of a spectrograph is:
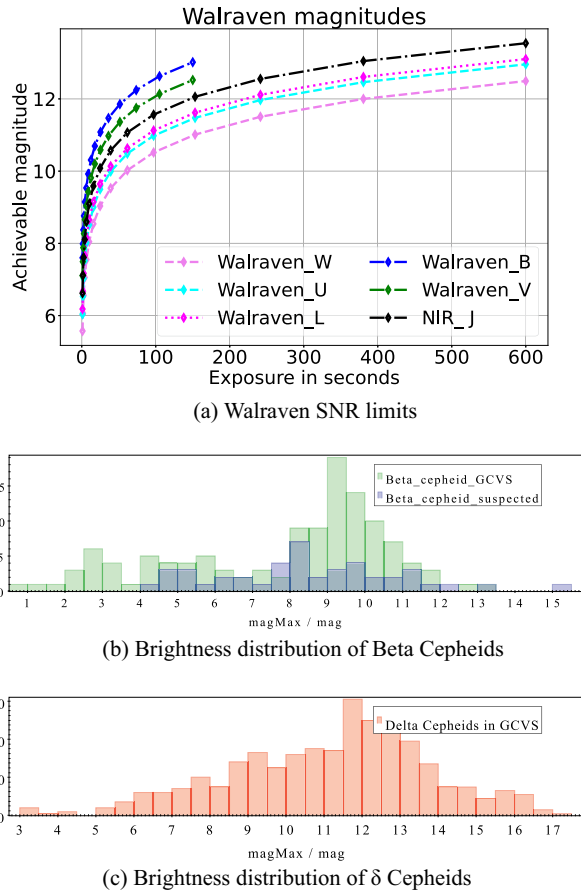
$$R = \frac{\lambda_c}{\Delta\lambda}, \tag{13}$$

where λ_c is the central wavelength and $\Delta\lambda$ is the smallest resolvable wavelength element. Which can be expressed as:

$$\Delta\lambda = \left[\frac{\lambda_{\text{span}}}{d_t}\right] \times \Delta S, \tag{14}$$

---

[16]https://www.shimadzu.com/opt/.

[17]https://spectrolamps.com/spectral-lamps/.

(a) Walraven SNR limits

(b) Brightness distribution of Beta Cepheids

(c) Brightness distribution of δ Cepheids

Figure 11. Limiting magnitudes versus integration time in the Walraven photometric system from a 1U aperture are shown in (a). Luminosity distribution (from GCVS, Samus *et al.* 2017) of a few β cepheids is shown in (b), and of classical cepheids is shown in (c). The magnitude limits are for a photon noise limited SNR of 100 and are calculated by assuming nominal values of throughput (typically 35–40%), quantum efficiency (50% in NUV and 70–80% in VIS-NIR). SED distributions are from (Fitzpatrick 2010) for NUV wavelength range and from (Zombeck 2006) for VIS-NIR wavelength range.

where λ_{span} is the total wavelength span which is mapped to a detector of size d_t and ΔS is the physical spot size along the direction of dispersion

$$\Delta S = \sqrt{(\Delta a)^2 + (\Delta d)^2 + (\Delta x)^2 + (\Delta p)^2}. \quad (15)$$

The physical size of the spot includes contributions from optical aberrations (Δa), diffraction (Δd), steering errors scaled by the platescale (Δx), and detector pixel size (Δp). Thus, the final resolution can then be written as:

$$R = \frac{\lambda_c d_t}{\lambda_{span}\sqrt{(\Delta a)^2 + (\Delta d)^2 + (\Delta x)^2 + (\Delta p)^2}}. \quad (16)$$

A relation between steering error and resolution is plotted in Figure 15 by taking an example of Hamamatsu S10141−1107S matched to the NUV spectrograph described in Figure 14(a). A nominal 1 arcsec of steering stability is desired to retain the original resolution at 3000. The corresponding guide camera (Figure 13) has a pixel-scale of 0.36 arcsec, therefore the total guiding error must be within 3 pixels to maintain this nominal resolution.

4.3 *Example science case: FUV/NUV spectroscopy*

For observing pulsating variables, FUV/NUV spectroscopy has regained recent interest. The variable star δ Cepheid has been observed by (Engle *et al.* 2014) to show strong emission lines in FUV which also vary in correlation with the pulsation phase. This definitely hints at a pulsation driven shock mechanism as the source. Such spectroscopic studies can be extended to a number of other variable stars if sufficient observing time can be allocated, such as from a CubeSat based platform. Of particular interest will be intermediate period Type-II cepheids, such as W Virginis which have been reported to show signatures of pulsation driven shocks in the form of emission lines in H-α (Kovtyukh *et al.* 2011). Similarly non-radial pulsators, such as β Cepheids which are inherently bright in shorter wavelengths will also be of interest for such studies. An estimate of achievable magnitude limits for a CubeSat based platform is shown in Figure 16(a) and a magnitude distribution of β cepheids is shown in Figure 11(b); demonstrating that a significant number of such sources should be within the capabilities of a 2U CubeSat.

We have assumed a Vega like Spectral Energy Distribution in our SNR analysis. In this regard, Fitzpatrick (2010) have reported slight anomalies (of the order of 5%) in the SED of Vega when compared to best fit theoretical models. They have recommended follow-up observation of a large number of similar A type stars to constrain whether the anomalies are unique to Vega or extend to other stars as well. This is also an important area where CubeSats can provide much sought after observations.

Since, CubeSat based platforms can only have limited aperture, it is absolutely essential to be efficient with the gathered photons. In this regard, the afocal slit-less spectrograph has a unique benefit. For low and medium resolution ($R < 5000$), the slit-less design has 'perfect' slit transmission – 100% compared to slit based systems where the typical slit efficiency can be around 60% – as well as better throughput (about 20% higher than conventional) as the collimator group is not

(a) Top view

(b) Side view

(c) Side view

(d) Side view
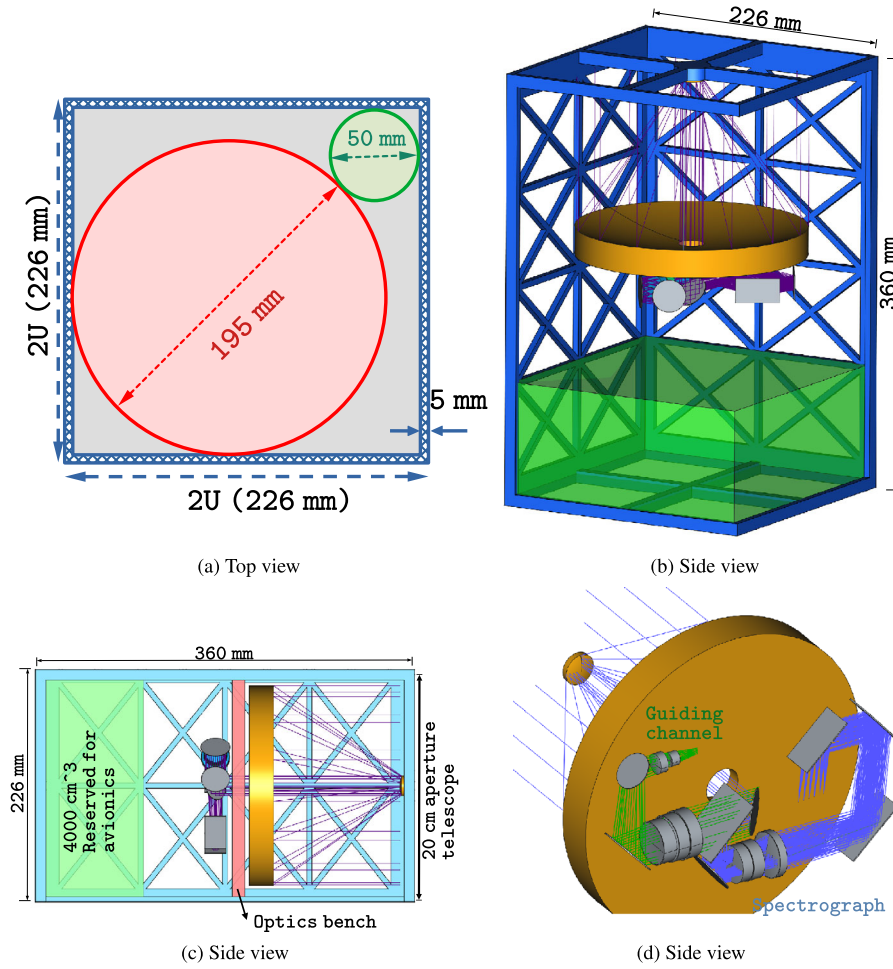
Figure 12.   Plan for a CubeSat observatory utilising a 20 cm (practically 195 mm) aperture telescope. The entire observatory fits within a 12U volume, of which about 8U is reserved for the optical telescope and components. Aperture distribution is shown in (a). Space distribution within the 12U volume is shown in (b) and (c). An illustrative combination of a guiding channel and a science channel (NUV spectrometer) is shown in (d). These optical designs are discussed in detail in Figures 13 and 14(a).

required. A comparison of afocal slit-less design and a conventional slit based design is presented in Figure 16(c). Improvement of about 0.5–0.7 magnitudes in terms of limiting magnitude may be expected for an afocal design. Throughput improvements resulting from afocal slit-less design is complemented well by the good quantum efficiency of modern CCD detectors (typically about 50–60% compared to only 20–30% of MCP type detectors) as well as specialised coatings in the UV (e.g., Woodruff *et al.* 2019); thus allowing a broader scope for CubeSat based spectrographs.

Imaging cameras in the 2U template

In Figure 17, a number of imaging cameras based on the 2U template are shown. Again, all designs share

the same afocal telescope. Figure 17(a) presents an NUV imager in the wavelength range of 225–360 nm. The design is implemented with MgF2 and Fused silica glass; a total of 6 lenses are used. The imager is optimised for a 21 arcmin field of view. The corresponding spot diagram is shown in Figure 17(b). The imager has an F10 output and produces an image circle of about 13 mm. Detectors, such as the IMX487 or GSENSE2020BSI, will be a good match for this. With IMX487, the pixel scale is about 0.3 arcsec. The design in Figure 17(c) is a fully reflective camera based on the Three Mirror Anastigmat (TMA) design. As the name suggests, three off-axis mirrors are used to realise a camera. The design is optimised for a field of view of about 12 arcmin and produces an image size of 14 mm. The spot diagram for this design is shown in Figure 17(d). As the design only uses reflective components, this camera

(a) 2U guiding camera   (b) Spot for 2U guiding camera
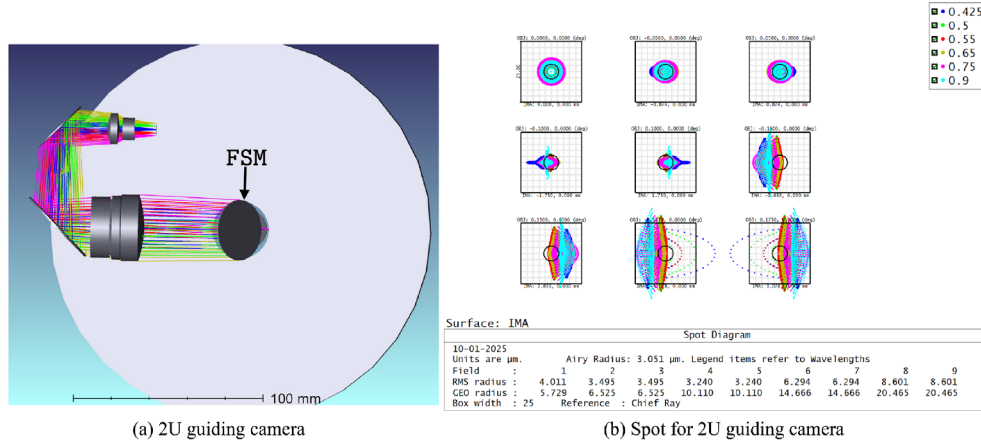
Figure 13. 2U guider camera: layout for a guide camera for the 2U design template is shown in (a). The guide camera is dichroically split from the main science camera. The camera design is done keeping the IMX477 sensor (similar to the 1U guiders) and has a fairly fast F5 output to accommodate the small 1.55 micron pixels of the sensor. The field of view is about 24 arcmin. The imaging performance of the camera is shown in (b), showing reasonably good optimisation for the required field of view. The sensitivity limit of this camera is shown in Figure 7 and the probability of finding a guide star is listed in Table 1.

can be used for a wide range of wavelengths. In particular, this design will be useful as an FUV camera suited for detectors like S7170−0909 from Table 3.

5. A few illustrative science cases

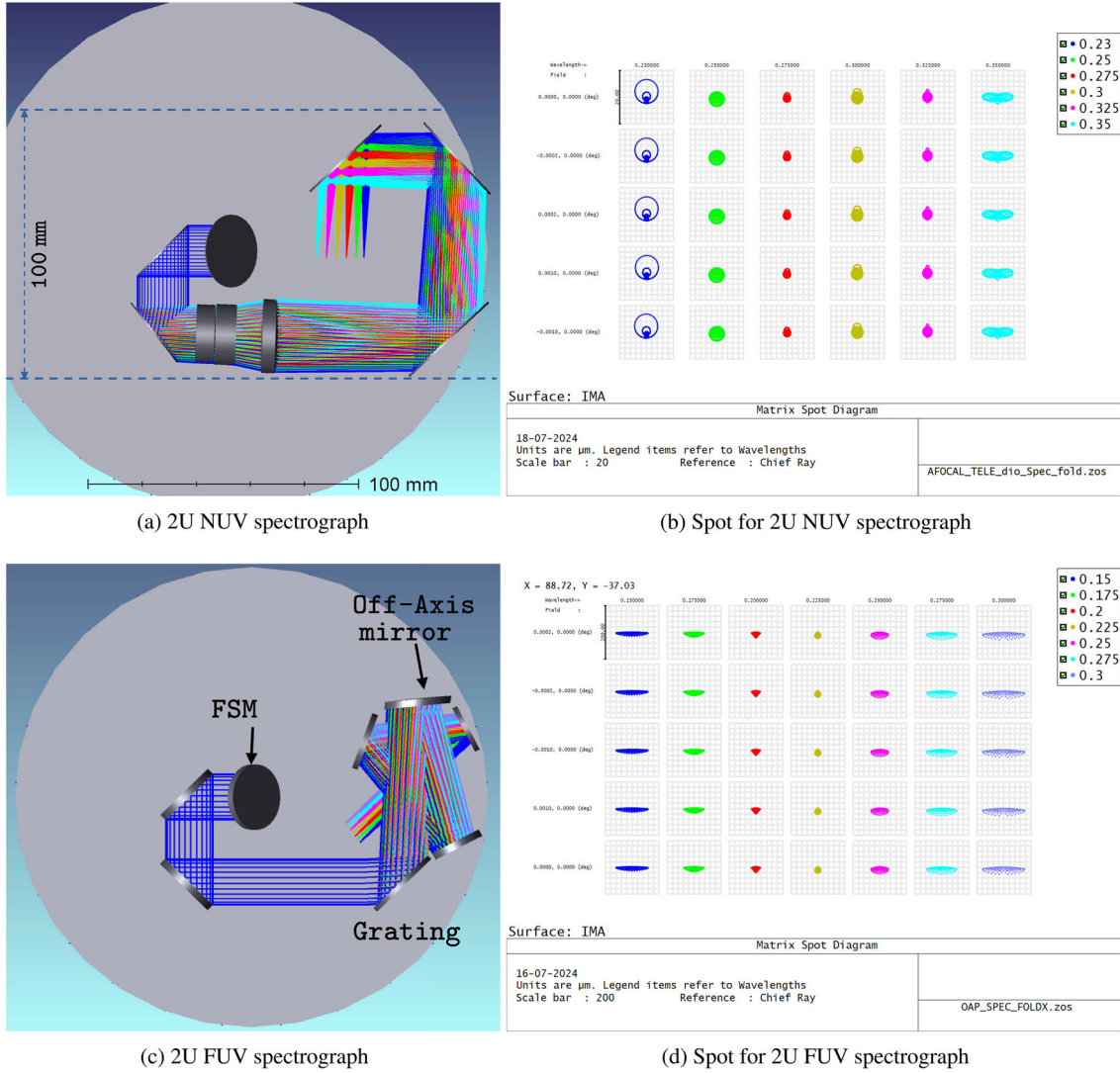### 5.1 *Multi-wavelength asteroseismology*

In recent times, significant insights have been made into stellar structure and evolution owing to progress in asteroseismology (Aerts 2021). However, most of the asteroseismology has been done in missions, such as TESS (Ricker *et al.* 2015), where the observation is through broadband filters optimised for exoplanet detection. The concept of astero-seismological modes may naturally be extended to shorter wavelengths for early-type stars. As the radiant flux of these stars is higher in the shorter wavelengths, it is also possible that the amplitude of the modes is higher in these wavelengths. The nature of observation (of continuous data over long durations) will also reveal the nature of flaring and related activity of these stars.

Similarly, it will also be useful to see the behaviour of pulsating variables in the infrared wavelength range. Particularly, infrared light-curves are important as they are inherently a better indicator of the period-luminosity law of these sources. From a small aperture CubeSat it will be possible to cover a large number of bright infrared sources and their variability can be studied at good time resolution. Additionally, since pulsating variables are typically evolved stars, their radiant flux increases as wavelength is increased, and hence there is a significant scope of detecting astero-seismological modes of these sources in the infrared. Currently, modes in the infrared range are not very well understood, and some very unique opportunities remain in this type of detection (Kallinger & Weiss 2005).

5.2 *Emission line stars*

Emission line stars, such as classical Be stars (Rivinius *et al.* 2013) and more exotic variants thereof (Bhattacharyya *et al.* 2021; Wang *et al.* 2022) – present opportunities for study of some very unique astrophysical phenomena, such as circumstellar disc formation, dissipation, and many others (Porter & Rivinius 2003; Rivinius *et al.* 2013). Dedicated monitoring of these sources can reveal a significant amount of information regarding the characteristics of the disc (Banerjee *et al.* 2022, 2024) and the evolution of the central massive star. However, ground-based observations remain at the mercy of weather and geographical constraints. A CubeSat based platform can provide continuous observations of these sources. In this capacity, the 1U observatory template discussed previously (sub-section 4.1) is of particular interest as it can provide simultaneous photometric observations in a wide wavelength range (NUV–NIR). This is crucial to understanding the evolution of different components of the circumstellar disc at different timescales. It is also expected that NUV photometry can be used as an indicator of activity in the

(a) 2U NUV spectrograph

(b) Spot for 2U NUV spectrograph

(c) 2U FUV spectrograph

(d) Spot for 2U FUV spectrograph

Figure 14. Review of 2U spectrographs: Layout of a NUV and a FUV spectrograph is shown in (a) and (c). The NUV spectrometer covers 230 to 350 nm and is based on a three-lens design. The spot diagram for the same is shown in (b), illustrating typical line spread within 15–20 microns. Similarly, the FUV spectrograph covers 150 to 300 nm in wavelength range, and has a reasonable line spread as shown in (d). Both of these designs are to be used with the guider design shown in Figure 13 and use the same afocal telescope, i.e., the same primary and secondary combination.

disc and hence as a trigger for ground-based follow-up observations.

The numerous emission lines seen in the spectra of these stars (Mathew & Subramaniam 2011; Banerjee *et al.* 2021) are also diagnostic tools for the circumstellar disc as well as the central massive star. In this regard, NUV spectroscopy will provide an additional tool that is yet to be explored to understand and characterise different line-forming regions in Be stars and thus investigate the evolutionary status of such systems. It will be interesting to match the NUV spectral features to that of emission lines in terms of line profile and

variability at different epochs. Overall, it is expected that an approach combining ground based and CubeSat facilities can provide new insights as well as broaden the scope to include other similar variables, such as Ae stars (Anusha *et al.* 2021).

5.3 *Spectropolarimetry*

Afocal designs allow for the implementation of fully rotationally symmetric cameras, resulting in low instrumental polarization. Additionally, the compactness (by skipping the collimator group) of these designs make
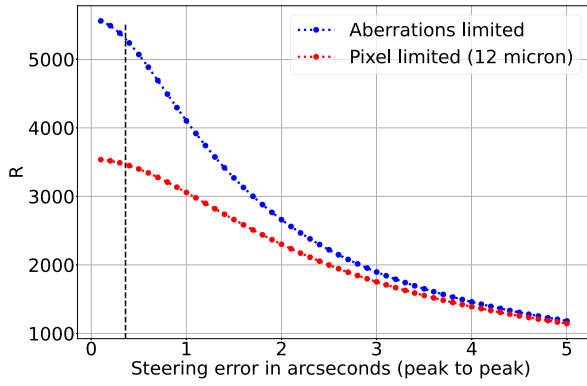
Figure 15. For slit-less spectroscopy, the final resolution is dependent on the steering error. Expected degradation in resolution is shown. It is to be noted that the plot includes other effects, such as pixel size, optical aberrations, etc. The discussed NUV spectroscope is actually pixel size limited and can maintain this resolution if the steering error is kept <1 arcsec. The black vertical line shows the pixel scale of the guiding camera.

them good candidates for CubeSat based polarimetric observation. An illustrative example is shown in Figure 18(a). In the example, an RC telescope has been used as the camera, but it should be possible to implement this with a Gregorian telescope or even a monolithic telescope. The fine pointing stability is achieved by using an X-Y stage, such as from Table 3, to match the exact F-number. There have been examples of upgrading an existing collimator camera design with polarimetric capabilities by introducing an Wollaston prism in the collimated beam-section (e.g., Helhel *et al.* 2015). This design is usable in a wide wavelength range (200–1700 nm) and can utilise both a GRISM or a zero-deviation prism (e.g., Hagen & Tkaczyk 2011) for dispersion and a Wollaston prism (e.g., Oliva 1997) for separation of orthogonal polarimetric components. The required parameters of the the dispersing and polarization element can be inferred directly from the geometry of the afocal design.

Let us consider a primary diameter D_P, a beam compression ratio C, and a final f-number of F_n. Then the focal length of the camera optics is given as:
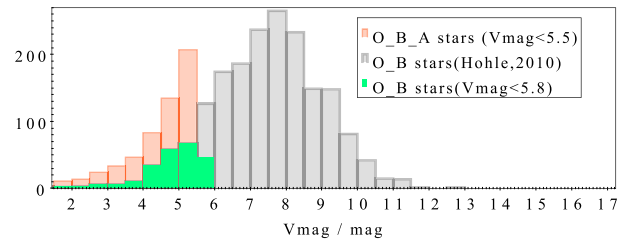
$$F_{\text{camera}} = \frac{D_P F_n}{C}. \tag{17}$$

If a Wollaston split of d_W (in mm) is to be achieved at the image plane, then the separation angle W_S (in degrees) of the Wollaston prism must be:
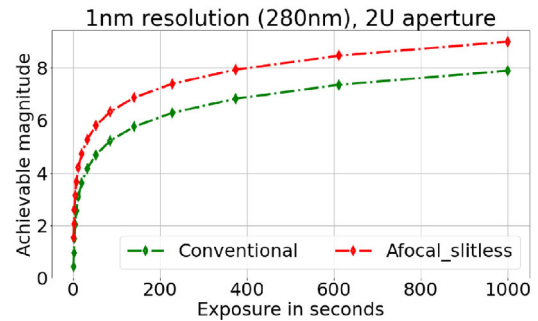
$$W_S = \frac{206265 \times d_W}{F_{\text{camera}} \times 3600} = \frac{57.3 \times d_W \times C}{F_n \times D_P}. \tag{18}$$
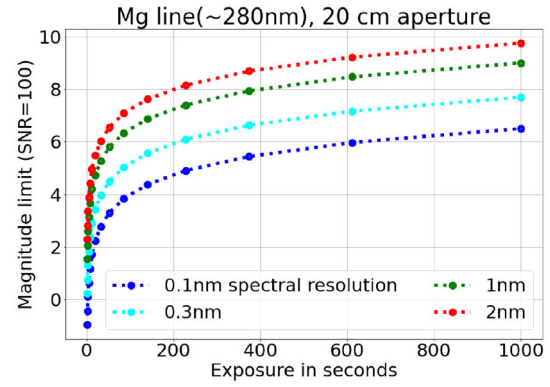
(a) Achievable magnitude limits for 2U aperture

(b) Brightness distribution of O and B type stars

(c) SNR advantage with an Afocal slit-less spectro graph

Figure 16. Limiting magnitudes shown in (a) are for an SNR of 100. The estimations are for nominal efficiencies, such as 50% detector quantum efficiency, 60% grating efficiency and 25% optical throughput. The spectral energy distribution is collected from Fitzpatrick (2010). In (b) the luminosity distribution of early type stars (from Hohle *et al.* 2010 and Warren Jr & Hoffleit 1987) is presented. Finally in (c) the throughput advantage of an afocal design when compared to a conventional design is shown.

Similarly, the desired dispersion (in degrees per nm) from the dispersing element is:

$$\text{Dispersion} = \frac{57.3 \times C \times d_\lambda}{F_n \times D_P \times \lambda_S}, \tag{19}$$

where λ_{span} is the desired wavelength span (in nm) and d_λ is the linear size of the dispersed spectra at the image plane. Necessary equations for estimating spectral resolution are already presented in sub-section 4.2 (Equations 13–16).

(a) 2U NUV imager

(b) Spot for 2U NUV imager

(c) 2U TMA imager imager

(d) Spot for 2U TMA imager
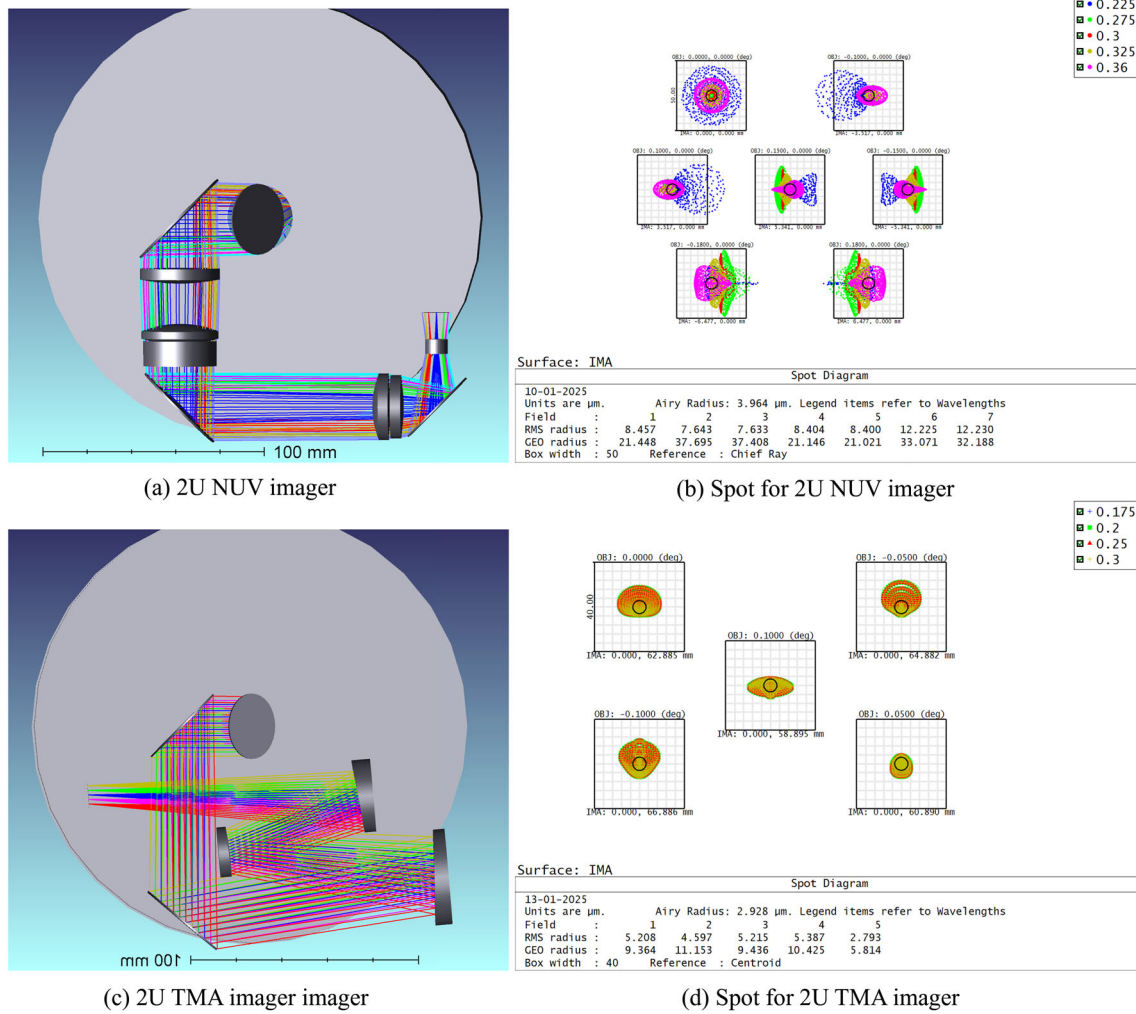
Figure 17. Review of 2U imagers: layout of a NUV imager is shown in (a). The NUV imager has a F8 output and a field of view of about 21 arcmin. The imaging performance of the same is illustrated in (b). In (c) a fully reflective camera based on TMA design is shown, and the corresponding spot diagram for 12 arcmin field of view is shown in (d). It is seen that the TMA type imager is close to diffraction limited whereas the refractive NUV imager is not. This is partly due to the presence of strong chromatic aberration in the NUV imager.

The expected limiting magnitudes are shown in Figure 18(c). The estimations are based on relatively conservative estimates of throughput (with details in the figure caption). The magnitudes may be compared to the luminosity distribution of O and B-type stars, as shown in Figure 16(b). It is exciting to note that there are sufficient number of bright O and B stars to probe the interstellar polarization even from a small aperture telescope. It may be possible to probe different regions of sky along with different distance ranges. The implementation of the camera with all reflective designs (such as the RC, Gregorian) or the monolithic camera allows for a wide range of wavelengths to be accessible within one instrument. This allows for low resolution spectro-polarimetry over a large enough spectral range to discuss the nature of Serkowksi curves (Papoular

2018) and perhaps its variability indicating composition of the interstellar medium at different directions.

## 6. Practical aspects of afocal designs

A number of practical aspects related to realization of CubeSat based observatory templates are discussed.

6.1 *Tolerancing and athermalization*

CubeSat designs typically require tight tolerance limits (typically 5 μm or less; e.g., CUBESPEC). This is inadvertently related to using fast telescopes in a space-constrained design as well as the necessity to

(a) Afocal Spectropolarimeter implementation by an RC type camera

(b) Spectropolarimeter spot

(c) SNR limits
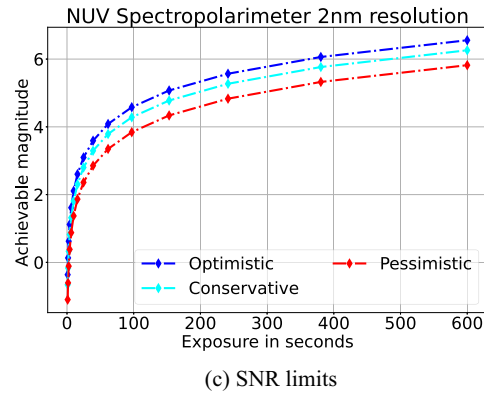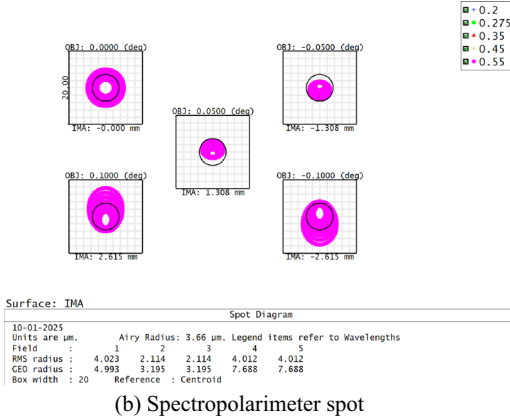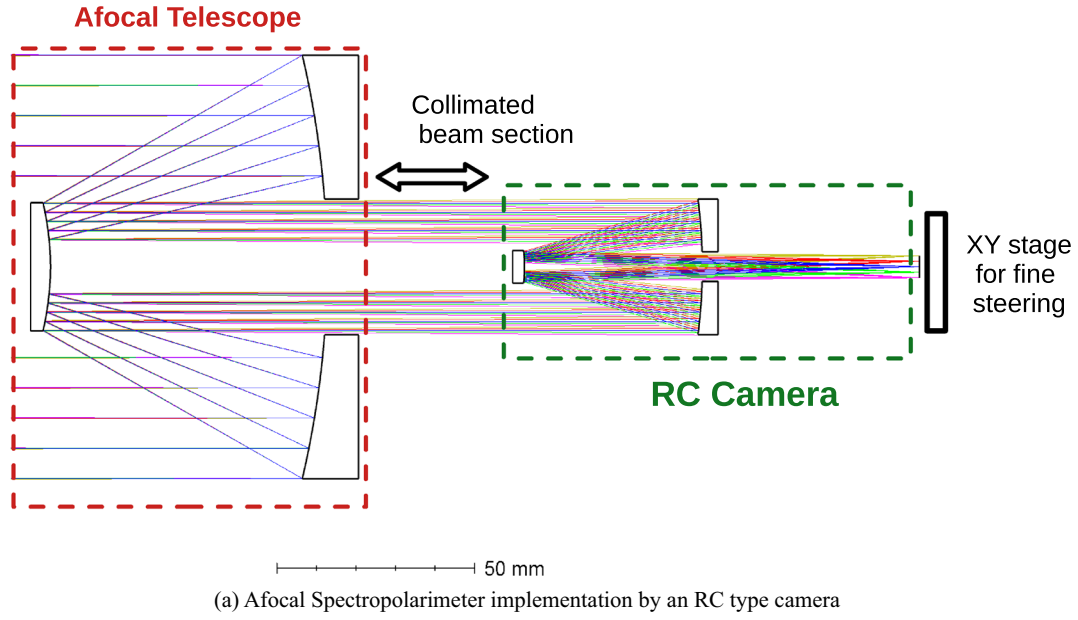
Figure 18. A fully rotationally symmetric afocal implementation: an interesting implementation utilising an afocal telescope is shown in (a). The complete imaging chain is fully rotationally symmetric so as to reduce instrumental polarisation. The fine pointing stability is achieved by using an X-Y stage, such as from Table 2, to match the exact F-number. The design achieves fairly good imaging performance as shown in (b) while implemented with all reflective components. The desired characteristics of the Wollaston as well as the dispersing element can be estimated by using Equations (17)–(19). Expected magnitude limits from a 10 cm CubeSat for the NUV wavelength range are shown in (c). Throughput and quantum efficiency assumptions remain the same as in Figure 16. The Wollaston efficiency is further split into optimistic (0.4), conservative (0.30), and pessimistic (0.2).

athermalise the design against thermally induced defocus. One aspect of afocal designs can help alleviate this issue: in an afocal design, the telescope and the camera are essentially decoupled from each other and can tolerate some amount of defocus (a few mm) and decenter (about 100 microns) without degrading the final image performance. This is a natural outcome since the coupling between the telescope and the camera happens within a collimated beam section. This allows for some amount of flexibility in the alignment of the complete system, as the telescope and the camera can

now be aligned separately and then assembled with the at a loose tolerance. The telescope itself still has to be aligned and athermalised. This can be done using standard opto-mechanics suitable for an RC telescope. Typically, the mechanical structure has to be of very low expansion material, such as invar or zerodur, to satisfy this requirement.

Specifically for the 2U template design discussed, the implementation of the FSM allows for one additional convenience in terms of alignment. Some amount of initial tilt between the optical bench and the afocal

Table 4. Tolerancing estimates for various designs. According to Edmund Optics' high-precision standard. Paraxial focus is used as the compensator.

Optical design	Original (μm RMS)	Tolerance (μm RMS)	Compens. (mm)
1U (Guider)	1.6	2.7	±0.35
1U (Vis)	3.8	7.5	±0.7
1U (NIR)	4.8	9.4	±1.7
1U (Greg.)	5.5	9.3	±4
2U (Guider)	5.1	9.7	±0.7
2U (NUV Spec.)	3.1	8	±2

telescope can be compensated for by the FSM itself. This is possible since the FSM is the coupling element between the telescope and the optical bench. This is, of course, subject to the maximum stroke of the FSM. However, this does allow for all the optical components on the optical bench to be tested before assembly onto the CubeSat platform without worrying too much about relative alignment between the telescope and the optical bench. A summary of tolerancing (closely following the Edmund Optics high precision standard[18]) related image degradation for various designs is presented in Table 4.

It should also be possible to make use of commercial off-the-shelf cameras along with the afocal telescope. Typically, cameras, such as from Schneider[19] or Nikon[20] (and many other manufacturers), which are designed for intermediate focal lengths (100–250 mm) and reasonably large apertures (>35 mm) will be a good match. The exact implementation will involve detailed knowledge of specific camera models regarding exact mechanical construction, number of elements, vignetting effects, and other factors. This is out of the scope of the present discussion.

6.2 *Natural modes of a sensitive structure*

It is of considerable importance that the natural vibrational modes within a space payload are identified. This is to ensure that no such modes are within the range of frequencies that may be excited during launch. Typically for CubeSats, modes below 100 Hz are best avoided (Herrera-Arroyave *et al.* 2016). Finite element analysis (using open-source Freecad[21] Calculix solver) is presented in Figure 19 for some of the critical components. The lowest excitation mode for a 12U frame is presented in Figure 19(a) and five of the lowest modes are listed. The frame is a structural component for the complete observatory. For simplicity, we have considered construction from 6061 Aluminium (with a weight of <3 kg). The frame is constrained at the launch rails and is evaluated while 'unfilled' (which is a worst-case scenario). The colour map identifies the mode (arbitrary units) and illustrates parts of the frame that are susceptible to this mode. A mesh convergence test is presented in Figure 19(b) to demonstrate repeatability of the analysis with respect to mesh density. Similar illustrative analysis is done for FSM mount (Figure 19c) and lens mounts (Figure 19d). The lens mount is tested without a lens; again, a worst-case scenario in terms of vibration. The preliminary analysis hints at a good margin of safety for these components. Of course, this type of analysis is more useful in highlighting problem areas and is not a substitute for rigorous physical testing.

6.3 *Laboratory test and characterisation of afocal systems*

Since the afocal telescope is also a beam expander/compressor with both input and output being collimated, it can be conveniently tested by means of optical interferometry. A simple setup based on a Twymann–Green interferometer (Malacara 2007) is shown in Figure 20(a). A reference collimated beam is given as input to the system. The input laser beam is required to be comparable in diameter to that of the secondary mirror only. The afocal telescope expands the beam further to fill its own primary mirror; hence, only a smaller collimated beam is required. This can be conveniently generated from off-the-shelf He-Ne laser beam expanders (e.g., see footnote[22]). One arm of the interferometer contains a reference mirror, and the other arm contains the telescope under test. A larger flat mirror is placed in front of the telescope to reflect both reflected beams. Both reflected beams are combined by the beamsplitter and interfere at the output at position B in the diagram. Since the afocal telescopes are used in double pass, their wavefront aberrations are doubled and hence easily measurable.

Another testing method that can be realised is shown in Figure 20(b). This method can test the camera of the afocal design by itself or the complete system consisting
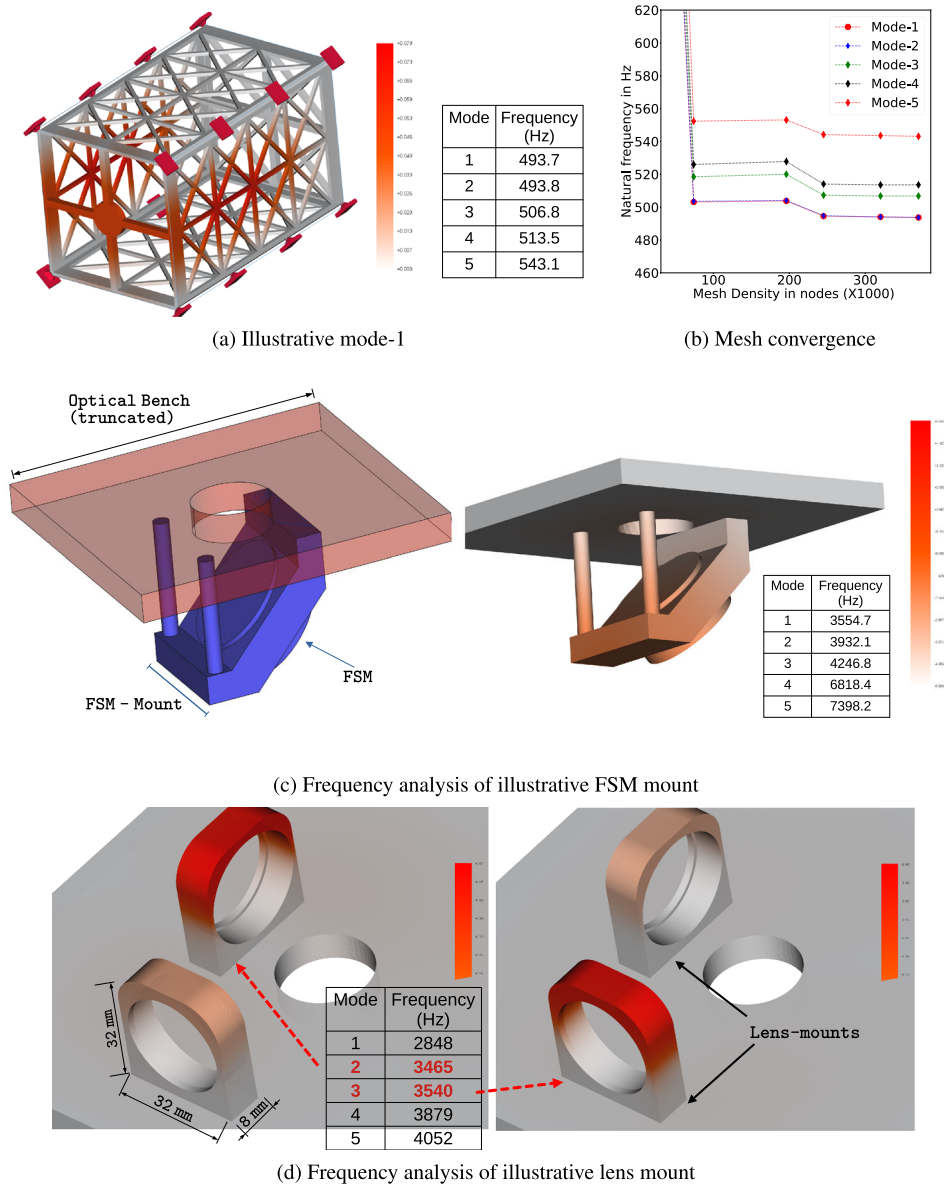
---

[18]https://www.edmundoptics.in/knowledge-center/application-notes/optics/precision-tolerances-for-spherical-lenses.

[19]https://schneiderkreuznach.com/en.

[20]https://www.nikon.com/business/industrial-lenses/lineup/.

[21]https://www.freecad.org/index.php.

[22]https://www.newport.com/p/T81-30X.

(a) Illustrative mode-1

Mode	Frequency (Hz)
1	493.7
2	493.8
3	506.8
4	513.5
5	543.1

(b) Mesh convergence

Mode	Frequency (Hz)
1	3554.7
2	3932.1
3	4246.8
4	6818.4
5	7398.2

(c) Frequency analysis of illustrative FSM mount

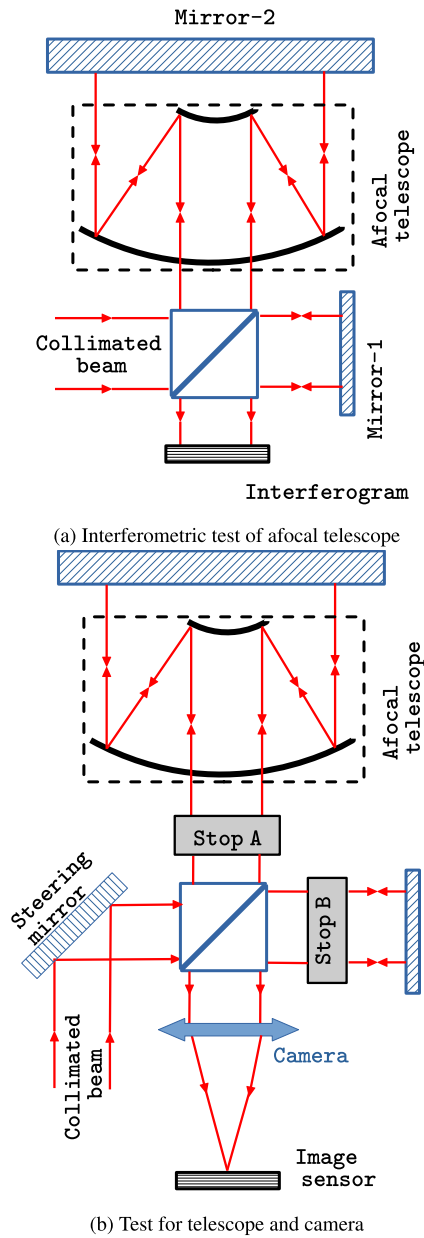| Mode	Frequency (Hz)
1	2848
2	3465
3	3540
4	3879
5	4052

(d) Frequency analysis of illustrative lens mount

Figure 19. Natural modes of vibration modes are identified for a few crucial structures. In (a), the lowest vibration mode of the 12U CubeSat frame is demonstrated. The mesh convergence of the same is shown in (b). The FSM mount (c) and lens mounts (d) are also analysed. All modes are well above 100 Hz, which is typically considered the minimum requirement for CubeSats. Instances of closely spaced modes are typically orthogonal modes in X and Y directions.

of the afocal telescope and the camera. Again, a reference collimator is required with a beam size comparable to that of the secondary mirror. This time, however, a broadband light source may be used. This collimated beam is diverted by the beamsplitter to two different arms. Depending on which arm is blocked or allowed, different parts of the system may be tested. If stop-A in the figure is kept in place and stop-B is removed, then only the camera optics is tested. If stop-B is kept in place and stop-A is removed, then the complete system is checked for image performance. The resulting image quality in either of the cases is observed at the output

of the camera optics, and hence, the system is mostly self-sufficient. The steering mirror, as shown in Figure 20(b), can be used to test the system for some amount of field of view. It should also be possible to switch the simple steering mirror to a functional FSM and test for static characteristics, such as stroke and precision of beam steering. It is of note that these test setups are realised mostly with 'generic' flat mirrors and do not require external calibration components, such as reference spheres. This is again one of the benefits of an afocal telescope towards reducing the time and cost of their realization.

Of course, the goal of a standardised and accessible CubeSat platform also requires coordinated effort from other areas, such as mechanical, electronic, communications, and system design. We hope that our work paves the way towards the ultimate aim of extensive utilization of CubeSat-based platforms by the astronomical community.

Acknowledgements

Appendix: Prescription table for guiding camera

Specifications of the guiding camera are attached (design in Figure 6c). The primary and secondary mirrors have a conic constant of -1.0 and -2.5, respectively. All lenses are spherical. This design serves as a common guiding camera optimised in the visible wavelength range. The design has an FOV of 40 arcmin and matches the commonly available Raspberry Pi HQ camera. See Table 5.

Table 5. Prescription data for the guiding camera, all glass types are from the Schott catalog.

Element	Glass	RoC (mm)	Thickness (mm)	Semidia (mm)
Primary	Mirror	-200.0	-75	50
Secondary	Mirror	-66.6048	-45	13.1
Lens-1	Fluorine	90.0909	5	9
	Crown	-111.3851	15	9
Lens-2	Boron	35.6488	5	6
	Crown	10.4333	3	5
Lens-3	Dense	-18.8786	5	4
	Flint	-21.0445	25	5

(a) Interferometric test of afocal telescope

(b) Test for telescope and camera

Figure 20. (a) Interferometric test of afocal telescope and (b) test for telescope and camera. Laboratory test setups: see text for details.

7. Concluding remarks

We have presented optical designs based on afocal telescopes in the context of CubeSat based astronomical observations. The practical advantages of these systems, such as standardisation and aberration-free beam steering, are discussed. It is expected that observatory templates based on afocal designs will result in a quick turnaround time and a reduction in development cost and efforts. A few science cases that can be accessed from such CubeSat-based platforms are also illustrated.

References

Aerts C. 2021, Reviews of Modern Physics, 93, 15001

Alarcon M. R., Licandro J., Serra-Ricart M. *et al*. 2023, Publications of the Astronomical Society of the Pacific, 135, 55001

Anusha R., Mathew B., Shridharan B. *et al*. 2021, Monthly Notices of the Royal Astronomical Society, 501, 5927

Auvergne M., Bodin P., Boisnard L. *et al*. 2009, Astronomy & Astrophysics, 506, 411

Bagnasco G., Kolm M., Ferruit P. *et al.* 2007, in Cryogenic Optical Systems and Instruments XII, Volume 6692, SPIE, p. 174

Baker J. G. 1969, IEEE Transactions on Aerospace and Electronic Systems, 261

Banerjee G., Mathew B., Bhattacharyya S. *et al.* 2024, arXiv preprint arXiv:2404.10339

Banerjee G., Mathew B., Paul K., Subramaniam A., Balan A. 2022, Journal of Astrophysics and Astronomy, 43, 102

Banerjee G., Mathew B., Paul K. *et al.* 2021, Monthly Notices of the Royal Astronomical Society, 500, 3926

Batty K., Steele I., Copperwheat C. 2022, Publications of the Astronomical Society of the Pacific, 134, 65001

Beals G., Crum R., Dougherty H. *et al.* 1988, Journal of Guidance. Control, and Dynamics, 11, 119

Betoule M., Antier S., Bertin E. *et al.* 2023, Astronomy & Astrophysics, 670, A119

Bhattacharyya S., Mathew B., Banerjee G. *et al.* 2021, Monthly Notices of the Royal Astronomical Society, 507, 3660

Candini G. P., Piergentili F., Santoni F. 2012, Acta Astronautica, 81, 325

Chandra P. B., Nair B. G., Jain S. *et al.* 2024, Journal of Astronomical Telescopes. Instruments, and Systems, 10, 26002

Chandra P. B., Nair B., Ghatul S. J. *et al.* 2024, Journal of Astronomical Instrumentation, 13, 2450005

Clermont L., Languy F., Georges M. 2020, Journal of Astronomical Telescopes. Instruments, and Systems, 6, 34003

De Maeyer J., Raskin G., Vandenbussche B., Vandepitte D. 2024, Journal of Astronomical Telescopes. Instruments, and Systems, 10, 34005

Dennehy C. J., Wolf A. A., Wu A. *et al.* 2020, Application of Micro-thruster Technology for Space Observatory Pointing Stability. Tech., Rep.

Douglas E. S., Tracy K., Manchester Z. 2021, Frontiers in Astronomy and Space Sciences, 8, 676252

Engle S. G., Guinan E. F., Harper G. M., Neilson H. R., Evans N. R. 2014, The Astrophysical Journal, 794, 80

Fitzpatrick E. 2010, The Astrophysical Journal, 725, 2401

Fleming B. T., France K., Nell N. *et al.* 2017, in UV, X-Ray, and Gamma-Ray Space Instrumentation for Astronomy XX, Vol. 10397, SPIE, p. 377

Flinois T. L., Haag C., Mandic M. *et al.* 2022, in Proceedings of the 44th Annual American Astronautical Society Guidance, Navigation, and Control Conference, 2022, Springer, p. 1415

Hagen N., Tkaczyk T. S. 2011, Applied Optics, 50, 4998

Hazra L. 2022, Foundations of Optical System Analysis and Design (CRC Press)

Helhel S., Khamitov I., Kahya G. *et al.* 2015, Experimental Astronomy, 39, 595

Herrera-Arroyave J., Bermúdez-Reyes B., Ferrer-Pérez J., Colín A. 2016, in 67th International Astronautical Congress. Mexico, Guadalajara, p. 1

Hohle M. M., Neuhaeuser R., Schutz B. F. 2010, Masses and luminosities of O- and B-type stars and red supergiants

Jin J., Zhang T., Kong L., Ma K. 2018, Sensors, 18, 106

Johnston-Lemke B., Sarda K., Grant C., Zee R. 2011

Kallinger T., Weiss W. W. 2005, in High Resolution Infrared Spectroscopy in Astronomy: Proceedings of an ESO Workshop Held at Garching, Germany, 18–21 November 2003, Springer, p. 443

Kimura S., Narumi T., Aoyanagi Y., Nakasuka S. 2015, Optical Payloads for Space Missions, 783

Kovtyukh V., Wallerstein G., Andrievsky S. *et al.* 2011, Astronomy & Astrophysics, 526, A116

Levchenko I., Bazaka K., Ding Y. *et al.* 2018, Applied Physics Reviews, 5

Liddle J. D., Holt A. P., Jason S. J., O'Donnell K. A., Stevens E. J. 2020, Nature Astronomy, 4, 1026

Lourie N. P., Baker J. W., Burruss R. S. *et al.* 2020, in Ground-based and Airborne Instrumentation for Astronomy VIII, Vol. 11447, SPIE, p. 2064

Mahajan V. N. 1998, Optical Imaging and Aberrations: Ray Geometrical Optics (SPIE press)

Malacara D. 2007, Wiley Interscience

Mandić M., Alvarez-Salazar O., Kiessling A. A. 2018, in Space Telescopes and Instrumentation 2018: Optical, Infrared, and Millimeter Wave, Vol. 10698, SPIE, p. 296

Mathew B., Subramaniam A. 2011, arXiv preprint arXiv:1108.5850

Mellier Y., Barroso J., Achúcarro A. *et al.* 2024, arXiv preprint arXiv:2405.13491

Milaševičius M., Mačiulis L. 2023, Aerospace, 11, 5

Mishra A. K., Kamath U. 2022, Journal of Astrophysics and Astronomy, 43, 13

Molinaro R., Ripepi V., Marconi M. *et al.* 2011, Monthly Notices of the Royal Astronomical Society, 413, 942

Morgan R. E., Douglas E. S., Allan G. W. *et al.* 2019, Micromachines, 10, 366

Nowak M., Lacour S., Lapeyrère V. *et al.* 2016, in Space Telescopes and Instrumentation 2016: Optical, Infrared, and Millimeter Wave, Vol. 9904, SPIE, p. 1507

Oliva E. 1997, Astronomy and Astrophysics Supplement Series, 123, 589

Onnembo A., Buonaura B., Caccin B., Russo G., Sollazzo C. 1985, Astronomy and Astrophysics (ISSN 0004-6361), Vol. 152, p. 349. Research supported by the University of Victoria, Ministero della Pubblica Istruzione, NSERC, and CNR

Ostaszewski M., Vermeer W. 2007, in New Developments in Optomechanics, Vol. 6665, SPIE, p. 96

Pain I., Stobie B., Wright G. S., Paul T., Cunningham C. R. 2003, in IR Space Telescopes and Instruments, Vol. 4850, SPIE, p. 619

Paluszek M. 2023, ADCS-Spacecraft Attitude Determination and Control (Elsevier)

Papoular R. 2018, Monthly Notices of the Royal Astronomical Society, 479, 1685

Peri L., De Maeyer J., De Munter W., Vandepitte D. 2023, in 13th European CubeSat Symposium, Date: 2023/12/11-2023/12/13, Location: Leuven (Belgium)

Poghosyan A., Golkar A. 2017, Progress in Aerospace Sciences, 88, 59

Pong C. 2018, in 32nd Annual AIAA/USU Conference on Small Satellites

Porter J. M., Rivinius T. 2003, Publications of the Astronomical Society of the Pacific, 115, 1153

Raskin G., de Maeyer J., Vandenbussche B. *et al.* 2022, in Space Telescopes and Instrumentation 2022: Optical, Infrared, and Millimeter Wave, Vol. 12180, SPIE, p. 1080

Ricker G. R., Winn J. N., Vanderspek R. *et al.* 2015, Journal of Astronomical Telescopes. Instruments, and Systems, 1, 14003

Rivinius T., Carciofi A. C., Martayan C. 2013, The Astronomy and Astrophysics Review, 21, 1

Rowlands N., Aldridge D., Allen R. *et al.* 2004, in Optical, Infrared, and Millimeter Space Telescopes, Vol. 5487, SPIE, p. 664

Samus N., Kazarovets E., Durlevich O., Kireeva N., Pastukhova E. 2017, Astronomy Reports, 61, 80

Sanders S., Taranta A., Mosor S. *et al.* 2012, in OFS2012 22nd International Conference on Optical Fiber Sensors, Volume 8421, SPIE, p. 75

Serjeant S., Elvis M., Tinetti G. 2020, Nature Astronomy, 4, 1031

Shkolnik E. L. 2018, Nature Astronomy, 2, 374

Smilo J., Ravizza F., Ganino J. *et al.* 2024, Deep Purple Payload Qualifies for NASA Launch, Could Provide New Method for Real-Time Space-Domain Awareness. Tech. Rep, Lawrence Livermore National Laboratory (LLNL), Livermore, CA (United States)

Sollazzo C., Russo G., Onnembo A., Caccin B. 1981, Astronomy and Astrophysics, Volume 99, p. 66. Research supported by the Consiglio Nazionale delle Ricerche

Sreejith A., Fossati L., Ambily S. *et al.* 2022, Publications of the Astronomical Society of the Pacific, 134, 114506

ter Horst R., Navarro R. 2024, in Advances in Optical and Mechanical Technologies for Telescopes and Instrumentation VI, Vol. 13100, SPIE, p. 1197

Terebizh V. Y. 2019, Survey Telescope Optics (SPIE press)

Van Amerongen S., Damen E., Groot M., Kraakman H., Van Paradijs J. 1987, Monthly Notices of the Royal Astronomical Society, 225, 93

Van Paradijs J., Van Amerongen S., Damen E., Van der Woerd H. 1986, Astronomy and Astrophysics Supplement Series (ISSN 0365-0138), Vol. 63, p. 71

Walraven T. 1952, MNASSA: Monthly Notes of the Astronomical Society of South Africa, 11, 36

Wang L., Li J., Wu Y. *et al.* 2022, The Astrophysical Journal Supplement Series, 260, 35

Warren Jr W., Hoffleit D. 1987, in Bulletin of the American Astronomical Society, Vol. 19, p. 733

Woodruff R. A., Danchi W. C., Heap S. R. *et al.* 2019, Journal of Astronomical Telescopes. Instruments, and Systems, 5, 24006

Yang C., Ji T., Li Z. *et al.* 2025, The Astronomical Journal, 169, 228

Zombeck M. V. 2006, Handbook of Space Astronomy and Astrophysics (Cambridge University Press)